2+2 = 3: Making Ternary Phases Through a Binary Approach

Andrew P. Justl, Giacomo Cerretti, Sabah K. Bux, and Susan M. Kauzlarich and Susan M. Kauzlarich

- 1. Department of Chemistry, One Shields Ave, University of California, Davis, CA 95616 USA
- 2. Thermal Energy Conversion Technologies Group, Jet Propulsion Laboratory, California Institute of Technology, 4800 Oak Grove Drive, MS 277-207, Pasadena, CA 91109
- *Corresponding author: smkauzlarich@ucdavis.edu

Abstract

Synthetic organic chemists have a large toolbox of named reactions to form structural motifs through a retrosynthetic approach, when targeting a complex molecule. On the other hand, a comparatively complex inorganic compound may be made through simple mechanochemical reactions of the elements followed by annealing. For complex phases that involve more than two elements, the simple mechanochemical process can be complex with many competing phases which can negatively impact desired properties. This point has been made recently with revelation of improved properties of thermoelectric materials upon removal of impurities. Compounds of the Yb₁₄AlSb₁₁ structure type represent complex Zintl phases with exceptional high temperature thermoelectric properties but are difficult to prepare in high purity. In this work, a quenching study was used to elucidate the pathway taken by reactions from the elements to form the complex ternary phase, Yb₁₄AlSb₁₁. Through that study, two Yb-Sb binary phases, Yb₁₁Sb₁₀ and Yb₄Sb₃, were identified as intermediates in the reaction. These two Yb-Sb binaries were investigated for use as reactive precursors to form Yb₁₄MnSb₁₁ in reactions with MnSb. Through this pseudoretrosynthetic approach, reactions from Yb₄Sb₃ allowed for the synthesis of high purity Yb₁₄MnSb₁₁ and Yb₁₄MgSb₁₁ through balanced, stoichiometric reactions. The apparent Yb₂O₃ $(\sim 1\%)$ impurity found in these products was systematically reduced with x in the series Yb₁₄- $_x$ MnSb₁₁ (x = 0 to 0.05), suggesting the main phase is inherently Yb-deficient and showing the high degree of control obtained through this synthetic approach. The stoichiometric sample of Yb₁₄MgSb₁₁ has a peak zT of 1.3 at 1175 K and the stoichiometric sample of Yb₁₄MnSb₁₁ has a peak zT of 1.2 at 1275 K. This approach to solid state synthesis provides reproducible products from balanced stoichiometric reactants to form high purity complex structure types and can be adapted to other difficult ternary systems.

Introduction

In the world of solution chemistry, mechanistic studies offer invaluable information about the reason certain reactions provide a desired result, and why others do not.^{1–6} Through a combination of experimental and computational studies the rationale behind unique aspects of a reaction pathway such as site reactivity or stereoselectivity can be elucidated.^{7,8} In addition to providing information about the reaction at hand, these studies can allow for the assessment of possible applications of the reaction to other systems. Because of the relatively low temperatures and self-contained nature of the solution reactions, taking aliquots for qualitative or quantitative evaluation through the course of the reaction is easily accessible in many cases.

Unlike many reactions performed in aqueous or organic solution, solid state synthesis is often done at high temperatures with reagents that can be incredibly reactive towards an increasing number of things, including common reaction vessels (SiO₂, Al₂O₃, etc.), as temperatures increase. Because of this, these reactions can often times be a black box where reagents are weighed, processed, and annealed to obtain a final product, but little is known about what occurs and what chemical species form before the final product is obtained. Gaining an understanding of what occurs throughout this process may uncover the relationship between phases, and lead to a more guided approach to synthesis. In addition to understanding the basic pathway of a reaction, detailed studies have provided the various precursor's roles in the final morphology and purity of the product.

The development of temperature dependent *in operando* techniques using X-rays, neutrons, and electron microscopy has helped to unveil the pathways some of these reactions take, but these experiments can also be limited by the reactivity of elements towards the capillary, atmosphere, or other aspects of the experimental setup.¹¹ Additionally, access to equipment with capabilities to reach the desired temperature ranges can be a limiting factor. More efforts into understanding the pathways complex solid-state reactions take could unveil new synthetic approaches and a route to higher purity products and new phases. Yb₁₄MgSb₁₁ is a Zintl phase whose unit cell can be seen in Figure 1. This complex phase contains 8 formula units per unit cell with each formula unit containing 13 Yb⁺² cations, 1 Yb⁺³ cation, 1 [MgSb₄]⁻¹⁰ tetrahedron, 1 Sb₃⁻⁷ linear unit, and 4 Sb⁻³ anions. Yb₁₄MgSb₁₁ and the isostructural Yb₁₄MnSb₁₁ both exhibit excellent high temperature thermoelectric properties and are under consideration for implementation in radioisotope thermal electric generators for space exploration.^{12–18} Because of the wide interest in thermoelectric modules for waste heat recovery, an efficient synthetic route to high purity phases with precise control over stoichiometry will have a significant impact on increasing the progress towards even higher efficiency materials.^{19–28}

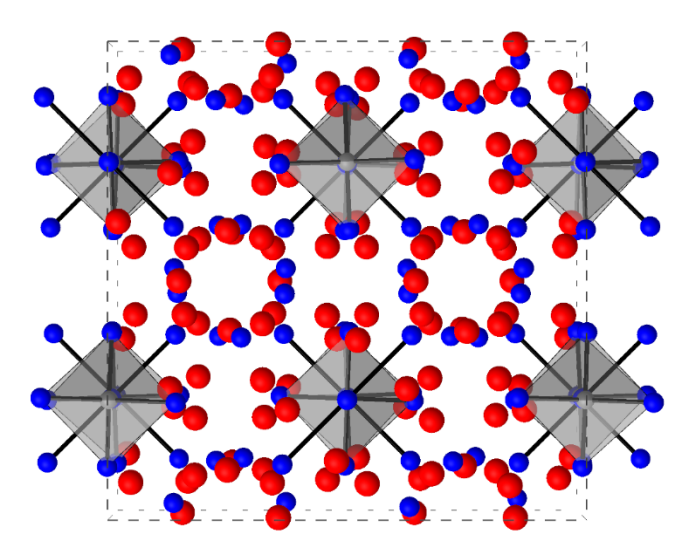


Figure 1. A view of the Yb₁₄MgSb₁₁ unit cell down the c-axis. Here, Yb is in red, Sb is in blue, and Mg is shown in grey.

In this work, a facile, accessible method for the study of reaction pathways to form the complex rare earth containing ternary phases Yb₁₄AlSb₁₁, Yb₁₄MnSb₁₁, and Yb₁₄MgSb₁₁ is presented. Two ytterbium antimonide binaries, Yb₁₁Sb₁₀ and Yb₄Sb₃, were investigated as reactive precursors in reactions with YbH₂ and either MnSb or Mg₃Sb₂ for guided synthesis of high purity products. We show that Yb₄Sb₃ is the best reactive precursor for preparing phase pure product and speculate on why that is the case. Based on this investigation, both Yb₁₄MgSb₁₁ and Yb₁₄MnSb₁₁ are determined to be slightly Yb deficient. The effects of Yb composition on the thermoelectric figure of merit, zT, for phases of Yb_{14-x}MnSb₁₁ are investigated and provide insight towards increasing the highest temperature thermoelectric properties.

Experimental

Quenching Studies. For reactions from the elements, Yb filings (Edgetech, 99.999%), Al filings (Alfa Aesar, 99.999%), and crushed Sb shot (5N Plus, 99.999%) were used. For reactions from the binaries, annealed binary phase powders were used. The binary powders were prepared as described below. Reactions were done with a total mass of 10 g in 65 cm³ stainless steel ball mills with two 12.7 mm diameter balls (SPEX). They were loaded in an Ar filled glovebox under inert atmosphere (<0.5 ppm O₂). Reactions were further jacketed in mylar baggies before they were removed from the glovebox and milled for three rounds of 30 minutes. The milling vials were flipped 180° after the first round and scraped with a chisel after the second. The resultant black powder was split into 10 portions, 9 of which were sealed under Ar in Nb tubes which were then further jacketed under vacuum in fused silica tubes to prevent oxidation of the refractory metal inner tube. The reactions were then placed in two box furnaces which have been programmed to the same heating rate (50 K / h) with an 8-hour offset between the two. An aliquot of the reaction was then quenched directly from the heating furnace into a large bucket of water every 100 K from 375 K to 1075 K and a final portion was left to anneal at 1075 K for 4 days. Portions of the reaction were then opened under inert atmosphere and analyzed by air-free powder X-ray diffraction to avoid oxidation of the finely divided particles or any metastable phases.

Powder X-ray Diffraction (PXRD). Samples of Yb₁₄MSb₁₁ (M = Mn, Mg, Al) as well as selected portions of the quenching study reactions were analyzed by powder x-ray diffraction (Bruker, Advanced Eco D8) on zero background off-axis quartz plates. A solvent smear using ethanol was used to plate samples of fully reacted Yb₁₄MnSb₁₁ and Yb₁₄MgSb₁₁. For the air-free patterns collected in the quenching study, double-sided Kapton tape (3M) or double-sided tape (ScotchTM removable double-sided tape, 3M) was used to create adhesion of the sample to the plating surface of an SiO₂ zero background holder. Once a thin film of the sample was dispersed onto the adhesive, a piece of Kapton film (XRF Window Film, Spex) was placed over the sample and sealed to the doubled-sided tape underneath. If sufficient bare adhesive is exposed on all sides of the sample film, a relatively air-tight packet can be created upon placement of the top film. The resultant powder patterns were analyzed by Rietveld refinements using the Jana 2006 software package.²⁹

<u>Synthesis of Binary Precursors</u>. Polycrystalline MnSb was made in 5g batches from the melt as previously described.³⁰ In an Ar filled glovebox (>0.5 ppm O₂), stoichiometric amounts of cleaned Mn pieces (Alfa Aesar, 99.95%) and Sb shot (5N Plus, 99.999%) were added to a BN crucible that was then heated to 1125 K for 12 hours in an evacuated fused silica ampule. After that period, magnetic, black crystallites were obtained. Due to the freshly cleaned Mn being used here, no Sb impurities were observed.

Powdered samples of Mg₃Sb₂ were made in 5 g batches through ball milling of the elements followed by annealing. In an Ar filled glovebox (>0.5 ppm O₂), stoichiometric ratios of Mg turnings (Strem Chemicals 99.8%) and Sb shot (5N Plus, 99.999%) were added to a 65 cm³ stainless steel ball mill with two 12.7 mm diameter balls. The reaction was then further jacketed in a mylar baggie before being removed from the glovebox and milled for four rounds of one hour each with a 15-minute break in between cycles. After four hours of milling a major phase of Mg₃Sb₂ could be identified by PXRD, but small Sb and Mg impurities remained. To complete the reaction the powder was sealed under Ar in a Nb tube and then further jacketed in an evacuated fused silica ampule. It was then annealed at 975 K for 12 hours. The resultant black powder was fully indexed as pure phase Mg₃Sb₂ with no impurities.

Both Yb₁₁Sb₁₀ and Yb₄Sb₃ were prepared by the same method of ball milling followed by annealing. In an Ar filled glovebox, Yb filings or small chunks (>3 x 3 x 3 mm) (Edge Tech, 99.999%) and crushed Sb shot (5N Plus, 99.999%) were added in stoichiometric ratios with a 10 g total mass to a 55 cm³ tungsten carbide ball mill with two 12.7 mm diameter balls. The mill was further jacketed in mylar baggies before being removed from the glovebox and milled for three rounds of 30 minutes each. The ball mill was scraped using a chisel in the glovebox after every 30-minute cycle. This step is important to reintroduce cold welded Yb into the bulk of the reaction and help lessen the amount of the Yb deficient side phase seen in the final product. After milling, the homogenous, black powder was sealed in a Nb tube under Ar that was then further jacketed in SiO₂ as described above. The reactions were then annealed at 1125 K for 12 hours. The resultant black powders could be indexed fully as a majority of the desired Yb-Sb phase with a minority impurity of the adjacent Yb deficient phase relative to the target. This minor impurity is due to Yb loss to the mill, but because the reaction can still be represented as a single point on the phase diagram, it is treated as a homogenous mixture of the two phases. To correct for the stoichiometry

of the mixture, a simple weighted average using the mole fractions from Rietveld refinements can be used to find the actual composition of the obtained mixture. This calculated compositional value can be then used to balance the reaction below, eqn (1).

eqn (1)
$$Yb_{11-x}Sb_{10} + YbH_2 + 2+x Yb + MnSb \rightarrow Yb_{14}MnSb_{11} + 0.5 H_2$$

Alternatively, one can use a three variable, three equation system of equations to balance the reaction, eqn (2), where the coefficients a, b, and c come from the three equations below that. In this approach, one equation is used to fix the Yb quantity, one is used for the Sb, and the third fixes the mole ratios of the two Yb-Sb binaries according to the results from Rietveld refinements.

eqn (2) a Yb₄Sb₃ + b Yb₁₁Sb₁₀ + c YbH₂ + MnSb
$$\Rightarrow$$
 Yb₁₄MnSb₁₁ + c H₂
eqn (3) 4a + 11b + c = 14
eqn (4) 3a + 10b + 1 = 11
eqn (5) $\frac{\chi_{Yb4Sb3}}{a} = \frac{\chi_{Yb11Sb10}}{b}$

Eqn (3) sets the Yb content to 14; eqn (4) sets Sb content to 11 and eqn (5) related the Yb₅Sb₃ content to Yb₁₁Sb₁₀ through the corresponding mole fraction (χ).

Typical PXRD's of all binary phases are provided in Supporting Information (SI) Figures S1-5 with Rietveld refinements reported in Table S1.

Synthesis of Yb₁₄MnSb₁₁ and Yb₁₄MgSb₁₁. Yb₁₄MnSb₁₁ and Yb₁₄MgSb₁₁ were prepared by balancing the stoichiometric reactions and by utilizing the Yb-Sb and Mg-Sb or Mn-Sb binaries as described above. The reactions were balanced by one of the two methods described above. In Equations (1) and (2), a small amount of additional Yb is required to balance the reactions. In reactions from Yb₁₁Sb₁₀ the additional Yb required to balance the reaction was introduced as one equivalent of YbH2 and the rest was introduced as Yb filings. For reactions from Yb4Sb3 the entirety of the remaining Yb was introduced as YbH₂. The YbH₂ was originally purchased as Yb metal powder (American Elements, 99.999%) but was later identified as YbH2 by PXRD.31,32 This is a result of the processing used to produce the powdered Yb which typically involves a hydride intermediate from which the hydrogen is removed, leaving the zero valent metal. Due to incomplete dehydrogenation, YbH₂ was left as the product. In both cases, YbH₂ allows for the introduction of a very high dispersity Yb source which will decompose to Yb metal and a partially reducing H₂ atmosphere as the reaction is heated.³¹ Due to the production of flammable hydrogen gas, the amount of YbH₂ used in each reaction was kept below 1.5 mole equivalents (350 mg) in a 5 g reaction. In any reaction performed in a sealed system, the H₂ gas was treated as an ideal gas to calculate possible pressures at the highest temperatures. The maximum pressure should be within the limits of the reaction vessel. Some refractory metals (Nb, Ta) are effectively transparent to small molecules like H₂. In this case the fused silica tube is what is exposed to the overpressure of H₂ and its volume should be considered for calculations. In an Ar filled glovebox (<0.5 ppm O₂), stoichiometric amounts of the respective powders were weighed out to high accuracy and precision (± 0.0001 g) with a 5.0000 g total reaction mass. The powders were added to a 65 cm³ stainless steel ball mill (SPEX) with two 12.7 mm balls. The sealed vials were further jacketed in a mylar baggie before being removed from the glovebox. The reactions were milled for three rounds of 30 minutes each with the milling vial being flipped 180° in the mill after the first round, and a scrape with a chisel in the glovebox after the second round. The resultant black powder was transferred to a 12.7 mm internal diameter graphite die (Cal Nano) inside the glovebox. The die was then transferred into the chamber of a Spark Plasma Sintering instrument (Dr. Lab Sinter Jr., Fuji Corp.) and the chamber was evacuated (<15 Pa). Under active vacuum, the die was heated to 873 K for 4 minutes then held for 30 minutes to perform the reaction. The progress of the reaction can be monitored by the overpressure generated from the H_2 off-gassing from the powders which was observed beginning around 473 K and continues until the dwell temperature of 873 K after which chamber pressures returned to starting values. After dwelling for 30 minutes the temperature was increased to 1123 K over the course of 3 minutes and held for 20 minutes to further consolidate the sample. During the first dwell step, force was kept at 5 kN. After the increase to 1123 K, the force was increased to 6.5 kN. The resultant pellet is pure phase $Yb_{14}MSb_{11}$ (M = Mg, Mn) with a density >98% of its theoretical value. A slice of the pellet was taken and ground under inert atmosphere for analysis by PXRD as described above.

<u>Elemental Analysis</u>. The sample composition was analyzed by Z contrast using scanning electron microscopy (SEM, Thermo Fisher Quattro ESEM). Elemental distribution and total content were analyzed by energy dispersive spectroscopy (EDS, Bruker Quantax) using Yb₁₄MgSb₁₁ and Yb₁₄MnSb₁₁ single crystals as elemental standards.

<u>Hall Measurements and Van Der Paw Resistivity.</u> Resistivity and Hall carrier concentrations were measured at the Jet Propulsion Laboratory (JPL) using the Van der Pauw method with a current of 100 mA and a 1.0 T magnet on a specialized high temperature instrument.³³

<u>High Temperature 2-Probe Measurements of the Seebeck Coefficient</u>. The Seebeck coefficients were measured at JPL using a custom instrument which uses the light pipe method with tungstenniobium thermocouples under high vacuum.³⁴

High Temperature 4-Probe Measurement of the Seebeck Coefficient and Resistivity. The Seebeck coefficient and electrical resistivity were measured on a portion of the sample after measurement at JPL. The sample was shaped into a bar (approx. $10 \times 1 \times 3$ mm) and polished, so all sides were parallel. The Seebeck coefficient and the electrical resistivity were measured with an off-axis 4-probe arrangement using a Linseis LSR-3 instrument with Pt/Rh thermocouples interleaved with carbon film strips on the bar to prevent any reactions. The measurement was performed under static He atmosphere after 3 prior pump/purge cycles ($P_{min} < 20 \text{ mTorr}$) and heated in a high temperature IR furnace. A polished Zr ribbon was placed inside the susceptor to act as an oxygen sponge, protecting the sample integrity. The ribbon became blackened and brittle upon completion of the measurement.

Thermal Conductivity. Thermal diffusivity was measured on densified pellets using Laser Flash Analysis on a Netzsch LFA 475 Microflash under Ar flow. The fully densified pellet was sliced into a thin disk (>1.5 mm) and polished until a uniform level surface was achieved on both sides. The density of this disk was measured using the Archimedes method with toluene as the liquid. Heat capacity of $Yb_{14}MgSb_{11}$ was estimated using the molecular weight of the $Yb_{14}MgSb_{11}$ analog relative to $Yb_{14}MnSb_{11}$, where $C_p(Yb_{14}MgSb_{11}) = C_p(Yb_{14}MnSb_{11})$ x $MM(Yb_{14}MnSb_{11})$. Here, MM is the molar mass of the respective compounds. The

coefficient of thermal expansion for Yb₁₄MnSb₁₁ was used to estimate the temperature dependence of the density. These were all combined to give the total thermal conductivity according to the equation: $\kappa = D x C_p x d$ (D = measured diffusivity; $C_p =$ heat capacity adjusted for molar mass; d = the temperature-adjusted density from Yb₁₄MnSb₁₁). The second representation of the temperature dependence of the temperature dependence of the temperature dependence of the density. The second representation of the temperature dependence of the temperature dependence of the density. The second representation of the temperature dependence of the density of the total thermal conductivity according to the equation:

Results and Discussion

The Formation of $Yb_{14}AlSb_{11}$ from the Elements. To investigate the mechanism by which $Yb_{14}MSb_{11}$ (M = Al, Mn, Mg) compounds form, a quenching study of the chemical reaction to form $Yb_{14}AlSb_{11}$ from the elements was performed. Figure 2 shows the resulting PXRD as a function of temperature. The Al analog was chosen because it has the least amount of peak overlap with many of the binary phases in this region of phase space. The milled powder before heat treatment is shown at the bottom of the experimental patterns which are ordered according to the indicated temperature with a reaction heating rate of 50 K per hour. The milled powder does not contain any reflections which are identifiable as the starting elements but is best matched with Yb_4Sb_3 and $Yb_{11}Sb_{10}$, suggesting that it is a mixture of the two Yb-Sb binary phases. As temperature increases, the reflections associated with these two phases become more intense, indicating that the phases become more crystalline. At 600 °C new reflections, which can be attributed to the ternary $Yb_{14}AlSb_{11}$ phase, can be seen around 31° 20. After that point, the ternary phase continues to form and becomes more crystalline as the reflections from the binaries dissipate. The final product after 4 days at 800 °C shows a majority $Yb_{14}AlSb_{11}$ phase with a minor $Yb_{11}Sb_{10}$ impurity.

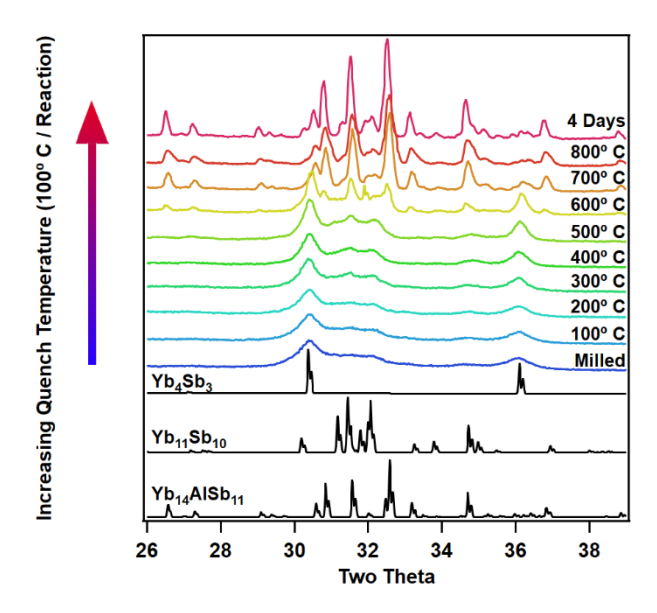


Figure 2. A variable temperature quenching study of the reaction to prepare polycrystalline $Yb_{14}AlSb_{11}$ from the elements. PXRD as a function of reaction temperature (indicated) with a heating rate of 50 K/h for milled powder of the elemental mixture: 14Yb + Al + 11Sb. Calculated diffraction patterns for $Yb_{14}AlSb_{11}$, $Yb_{11}Sb_{10}$, and Yb_4Sb_3 are provided.

The progression of this reaction can be understood through the principle of collision theory, which states that for two bodies to react, they need to collide with enough energy and in the correct orientation. Similarly, diffusion theory could be used to explain phase formation as diffusion can be described as the random movement of particles through space, usually due to a concentration gradient. In both cases an Arrhenius equation can be applied to explain chemical reactions. Figure 3 provides a schematic to show that the elemental reaction to produce a ternary phase initially consists of segregated particles of each element. The only region for a reaction to occur is at the interface of two of these particles. Ball milling of the elements inputs physical energy into the reaction. 35-37 Because the reaction is starting with elementally segregated particles, a maximum of two elements can exist at the interface of any two particles. This means that, at least initially, only binary phases can result at the interfaces of particles. Because the rates of collision between Yb and Sb particles are going to reflect the overall composition of the mixture, it would be expected that the phases forming would reflect that as well. Here the two binaries Yb₄Sb₃ and Yb₁₁Sb₁₀ are the result because Yb₁₄AlSb₁₁ resides between those two phases on a Yb-Sb binary diagram when not considering Al. Due to the low molar concentration of Al in this reaction, the rate of Al-Sb collisions, and in turn contribution to the formation of products, is near negligible. After milling, the mixture likely consists of small crystalline domains of binary phases along with unreacted amorphous regions. During annealing some of these small unreacted regions can react if the proper stoichiometry of elements is present locally. As temperature increases, these binary particles begin to increase in crystallinity and the interfaces between particles increase their complexity. What was once mainly interfaces of Yb and Sb is now interfaces of Yb-Sb binaries and particles of Al or Al-Sb. This interface now has all the elements required for the formation of the ternary phase. As temperature increases the possibility of collisions leading to the formation of the desired phase also increases, which is indeed what was observed at the higher temperature range in the study above.

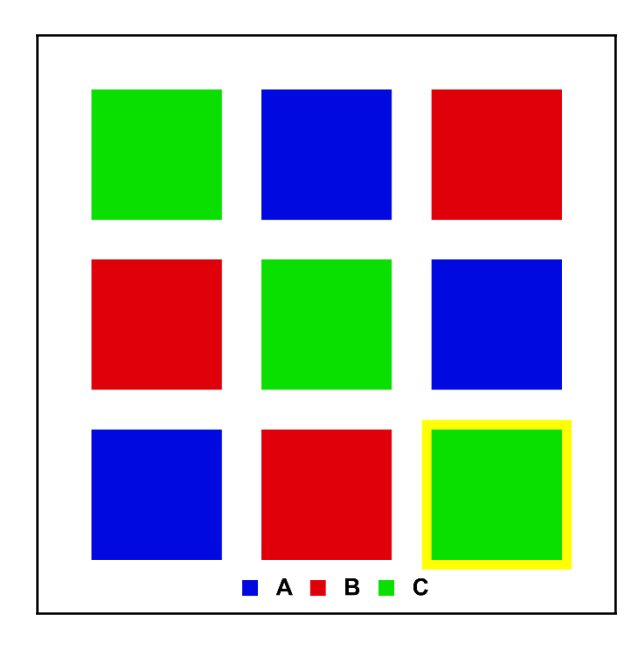


Figure 3. A schematic illustrating the interfaces of elemental grains for a reaction from the elements, A, B, C to form the ternary phase ABC. Each box is representative of a single particle/grain, one of which is highlighted in yellow for clarity.

One approach used for the synthesis of complex ternary phases is to avoid the formation of these binary intermediates altogether. ^{38–42} By depositing the elements into a thin, ordered film the diffusion path length of all the elements can be minimized. As this ordered amorphous film is then annealed, the layers react and directly form the desired ternary product with very high purity. Because each layer of the amorphous film is thin and the elements are layered in a specific order, there is effective control over the collisions at each interface. This approach is quite effective as it allows for the targeting of metastable phases which may not be as thermodynamically favorable as binary phases in the same region of phase space. Because Yb₁₄MnSb₁₁ is the most thermodynamically favorable phase within its region of phase space (Yb-Mn-Sb), it was investigated to determine whether those binary intermediates could be embraced rather than avoided to effectively lower diffusion path lengths and improve the overall purity of the product.

The Formation of Yb₁₄MnSb₁₁ from Yb₁₁Sb₁₀, MnSb, Yb and YbH₂. To investigate the possible reaction pathways polycrystalline Yb11Sb10 was prepared. Yb14MnSb11 was chosen as the synthetic target because of its excellent properties as a thermoelectric material in comparison to the Al analog. 15-17,30,43,44 Figure 4 shows the PXRD of high energy milled powder and after annealing of the constituents, Yb₁₁Sb₁₀, MnSb, Yb, and YbH₂, to make Yb₁₄MnSb₁₁. After milling, the reactants have gone from their crystalline forms to something more amorphous. The major reflections of Yb₁₁Sb₁₀ heavily overlap but can be identified as the broad peak observed between 30° to 33° 20. As the reaction heats to 400 °C, the peaks attributed to Yb₁₁Sb₁₀ become more crystalline in nature. At 500 °C reflections that can be attributed to the targeted Yb₁₄MnSb₁₁ begin to appear with intensities above the Yb₁₁Sb₁₀ reflections. The majority of the desired Yb₁₄MnSb₁₁ phase has formed 100 °C after the initial reflections appear. As the temperature is increased to 800 °C Yb₁₄MnSb₁₁ continues to become more crystalline, and the reflections attributed to the binary phases fade away. After 4 days at 800 °C the majority Yb₁₄MnSb₁₁ phase has formed with only minor impurities of Yb₂O₃ and Yb₁₁Sb₁₀. Taking a closer look at the diffraction patterns, the main diffraction peaks for Yb₂O₃ cannot be indexed in any pattern below 700 °C. This suggests that the oxide originates from a high temperature reaction possibly between unreacted Yb metal and the native oxide present on the interior of the Nb tubes. If this oxide was sourced from the Yb metal used, the oxide should be identifiable at lower temperatures. If this oxidation was due to significant amounts of oxygen gas present in the reaction vessel the oxidation of Yb metal would likely also happen at lower temperatures than what is shown here. Therefore, a likely hypothesis is that the thermite-style reaction between Yb and Nb₂O₅ has a sizeable activation energy which is why the oxide is not observed until higher temperatures. 45–47

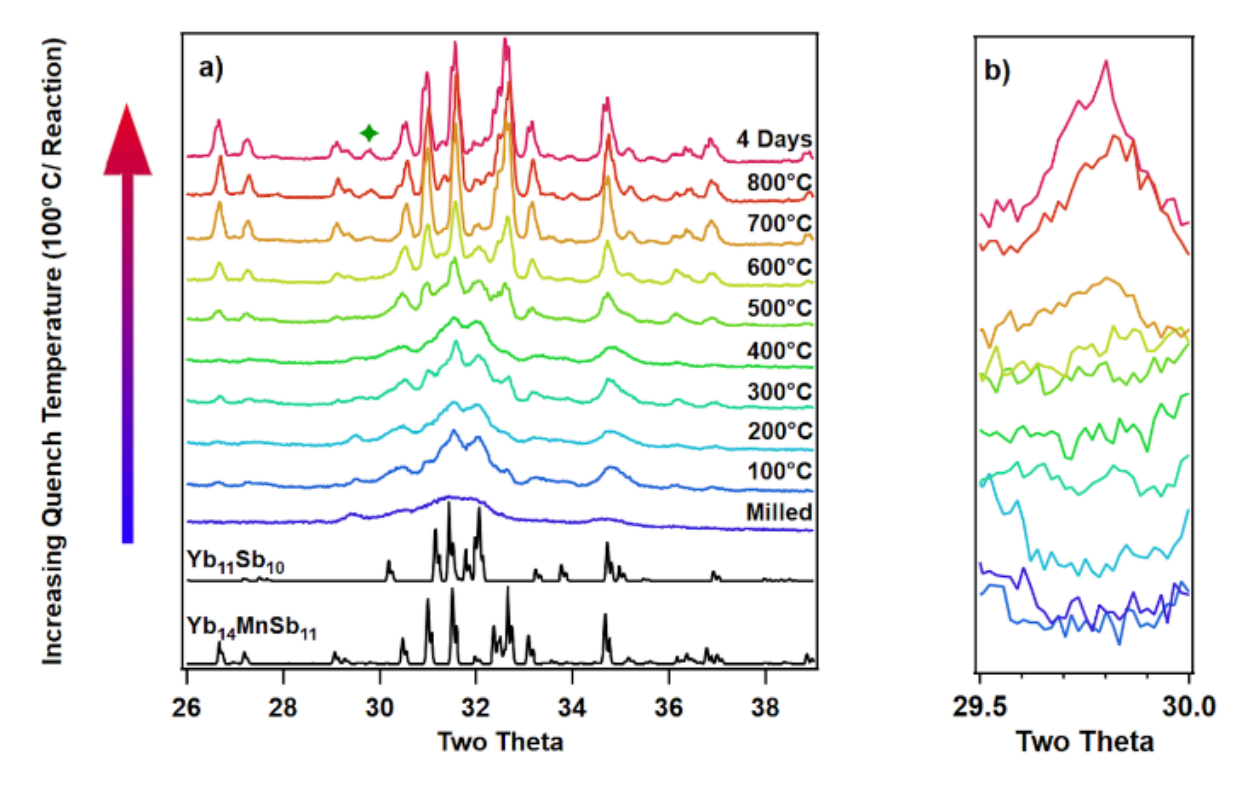


Figure 4. a) PXRD of a variable temperature quenching study of the reaction to form Yb₁₄MnSb₁₁ from a mixture of Yb₁₁Sb₁₀, MnSb, Yb, and YbH₂. Reference diffraction patterns for Yb₁₁Sb₁₀ and Yb₁₄MnSb₁₁ are shown in black on the bottom. b) An expanded view of the major Yb₂O₃ reflection which is marked by a green star in the full pattern. The color scheme is the same as that shown in a).

The formation of Yb₁₄MnSb₁₁ from Yb₄Sb₃, MnSb, and YbH₂. In a similar fashion to the study described above, polycrystalline Yb₄Sb₃ was prepared and the temperature study of the reaction to form Yb₁₄MnSb₁₁ is provided in Figure 5. Yb₄Sb₃ is the other Yb-Sb binary originally identified in the reaction from the elements for Yb₁₄AlSb₁₁.

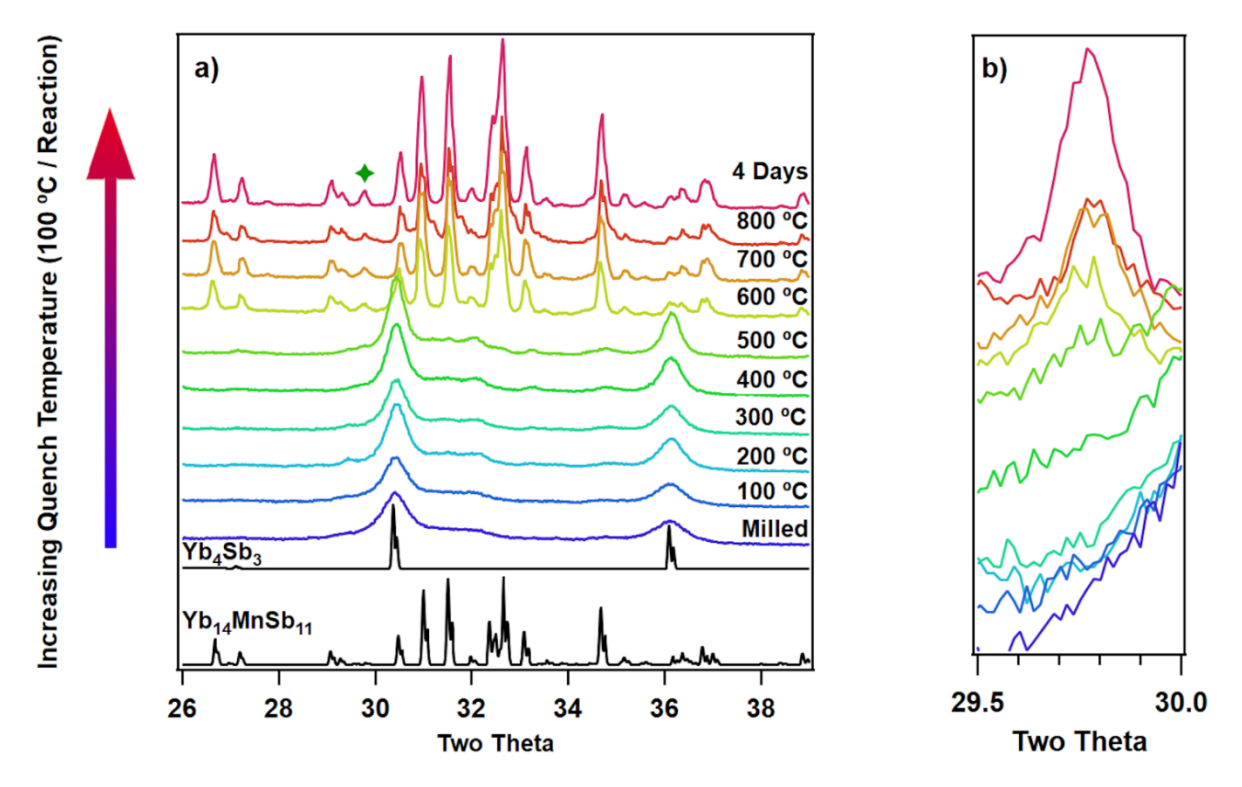
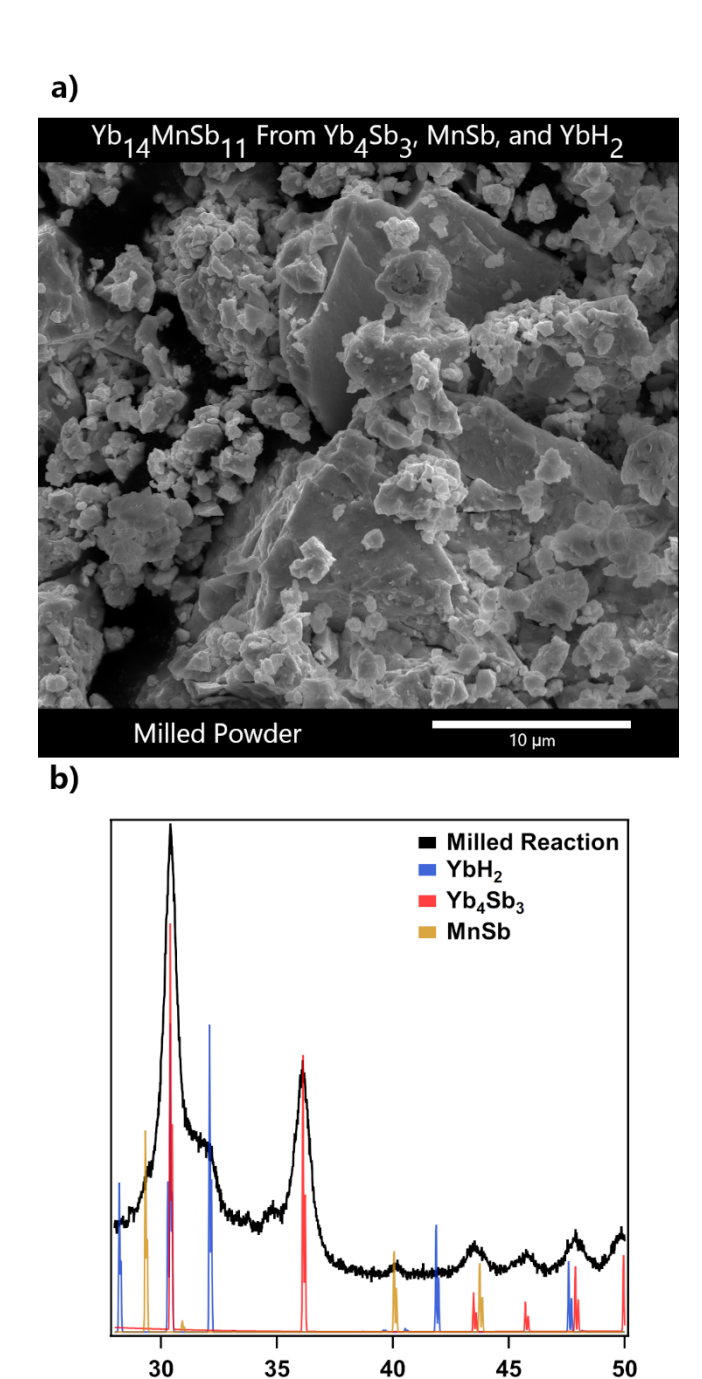


Figure 5. a) PXRD of a variable temperature quenching study of the reaction to form Yb₁₄MnSb₁₁ from a mixture of Yb₄Sb₃, MnSb, and YbH₂. Reference diffraction patterns for Yb₄Sb₃ and Yb₁₄MnSb₁₁ are shown in black on the bottom. b) An expanded view of the major reflection which is marked by a green star in the full pattern. The color scheme is the same as that shown in a).

After milling Yb₄Sb₃, MnSb, and YbH₂, the powder can be described as a mixture of amorphous material with very small crystalline domains much like what was observed in the reactions from Yb11Sb10. SEM micrographs (shown in SI Figure S6) show a mixture of particle sizes ranging from around 40 microns down to nanometer scale. Although there were larger sized particles, these contained several fractures, splitting them into smaller crystalline domains (Figure 6 a)). Unlike Yb₁₁Sb₁₀, which crystallizes in a tetragonal space group and has many reflections, Yb₄Sb₃ crystallizes in a cubic space group which lends to a simpler diffraction pattern with two main reflections around 30° and 36° 20. Because of this simplicity, reflections from YbH₂ were also able to be indexed in the milled powder, as shown in Figure 6 b), confirming that it does not decompose during the milling process. As the reaction is heated, the reflections from Yb₄Sb₃ become more intense and crystalline. Small reflections from the ternary phase Yb₁₄MnSb₁₁ can be identified around 33° 20 as low as 300 °C, but at 600 °C there is a drastic transformation from the mixture of binary phases to the targeted ternary phase. The Yb₁₄MnSb₁₁ continues to grow in crystallinity as the temperature increases to 800 °C. After 4 days at that temperature, the resultant product is pure phase Yb₁₄MnSb₁₁ with only a minor (~ 1 %) Yb₂O₃ impurity. Much like the reaction from Yb₁₁Sb₁₀, this oxide does not appear until elevated temperatures are reached, suggesting a high temperature reaction between Yb metal and an oxide containing species like the Nb₂O₅ native oxide that forms on the surface of the niobium tubes.



Two Theta

Figure 6. a) A scanning electron micrograph showing the fractures propagating through the larger particle in the bottom right. The scale bar is 10 microns. b) PXRD pattern of the milled powder of YbH₂, MnSb, and Yb₄Sb₃ to form Yb₁₄MnSb₁₁ with reference patterns for the respective reactants as calculated from ICSD data sets 43031, 54266, and 424602.

The differences in product purity between the three reaction studies described above can be understood through the lens of elemental distribution and loss. In the reaction from the elements, the resultant product was a mixture of $Yb_{11}Sb_{10}$ and $Yb_{14}AlSb_{11}$. In relation to $Yb_{14}AlSb_{11}$, the binary, $Yb_{11}Sb_{10}$, is Yb deficient with respect to the Yb-Sb relative atomic amounts. This suggests

that the undesired Yb₁₁Sb₁₀ side phase is a result of Yb deficiencies within the reaction mixture and that it is the result of Yb loss to the mill. This loss is hard to avoid in elemental synthesis due to the sticky nature of Yb metal and brings the overall reaction to a Yb deficient state. This deficient reaction then progresses by the reaction shown below.

$$14-x \text{ Yb} + \text{Al} + 11 \text{ Sb} \rightarrow \text{Yb}_{14} \text{AlSb}_{11} + \text{Yb}_{11} \text{Sb}_{10} + \text{Al}$$

In the case of the reaction from $Yb_{11}Sb_{10}$ to form $Yb_{14}MnSb_{11}$, the resultant product was a mixture of $Yb_{11}Sb_{10}$, Yb_2O_3 , and the desired $Yb_{14}MnSb_{11}$ phase. Here, there are both the Yb deficient phase $Yb_{11}Sb_{10}$ and the Yb rich phase Yb_2O_3 . The final mixture of these two phases with $Yb_{14}MnSb_{11}$, along with the formation of Yb_2O_3 at elevated temperatures, suggests that the reaction mixture was not homogenous. If the reaction consisted of small Yb rich and deficient regions, the deficient regions would progress by a similar reaction as outlined above. The Yb rich regions react to fully form $Yb_{14}MnSb_{11}$, due to a more favorable enthalpy of formation ($\Delta H_{Yb11Sb10} = -1.035$ eV, $\Delta H_{Yb14MnSb11} = -1.052$ eV), with residual unreacted Yb metal, as indicated in the reaction shown below. Yb metal is extremely susceptible to oxidation at high temperatures and therefore oxidizes and is identified as Yb_2O_3 , indicated in parentheses below.

$$(3 + x) Yb + Yb_{11}Sb_{10} + MnSb \rightarrow Yb_{14}MnSb_{11} + x Yb (Yb_2O_3)$$

Finally, Yb₁₄MnSb₁₁ was made in very high purity through a reaction from Yb₄Sb₃ with only a minor oxide impurity. This implicates the possibility of native Yb defects being present in the Yb₁₄MnSb₁₁ that is being formed.

$$2/3 \text{ Yb} + 10/3 \text{ Yb}_4 \text{Sb}_3 + \text{MnSb} \rightarrow \text{Yb}_{14-x} \text{MnSb}_{11} + x \text{ Yb} (\text{Yb}_2 \text{O}_3)$$

Figure 7 illustrates the interfaces of particles/grains of the two binary phases A₂C and B₂C to form the ternary phase ABC. Because this model reaction consists solely of binary particles/grains, the distribution of C within A and B is on an atomic level. As the binary phases employed are further from the desired target and more additional reactants are required, the elemental distribution with that reaction is more like that of reactions from the elements (Figure 3). Therefore, the reason the reactions from Yb₁₁Sb₁₀ and Yb₄Sb₃ do not lead to the same products (Yb₁₄MnSb₁₁ with Yb₁₁Sb₁₀ and Yb₂O₃ vs Yb₁₄MnSb₁₁ with Yb₂O₃) is attributed to the relative ratios of elements within the binary phases employed. The reaction employing Yb₁₁Sb₁₀ requires more additional Yb to balance. This introduces more segregated regions of Yb in the initial reaction and increases the probability of inhomogeneous regions of Yb and results in the corresponding impurities (Yb₂O₃ and Yb₁₁Sb₁₀) in the final product. This is not the case for Yb₄Sb₃ as the starting reagent, which results in a higher purity of the final product Yb14MnSb11 with about 1% Yb2O3. Although not as ideal as the ABC case presented in the model, Yb₄Sb₃ requires significantly less additional Yb to balance the reaction and is as close to the model as the phase diagrams allow. The ideal reaction is one in which both the number of elemental reactants and the total number of reactants are minimized.

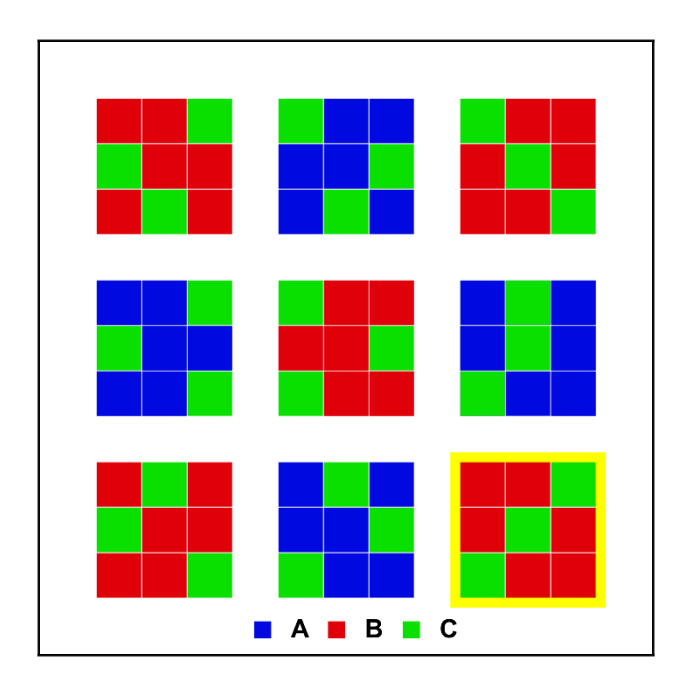


Figure 7. A schematic illustrating the interfaces of grains of binary phases of A₂C and B₂C to form the ternary phase ABC. Each box represents a single particle/grain of the binary phase, and one is highlighted in the bottom right for clarity.

Reactions to form Yb₁₄MgSb₁₁ and Yb₁₄MnSb₁₁ from the Binaries. Figure 8 shows the PXRD patterns of Yb₁₄MgSb₁₁ (red, top) and Yb₁₄MnSb₁₁ (blue, bottom) synthesized from Yb₄Sb₃, YbH₂, and either MnSb or Mg₃Sb₂ through ball milling followed by direct reaction through spark plasma sintering. Reference patterns for both structures are shown in black below the experimental patterns. 18,44 Yb₁₄MnSb₁₁ prepared from Yb₄Sb₃, YbH₂, and MnSb has lattice parameters of a =16.628(2) Å, c = 22.046(2) Å, and $V = 6096.0(4) \text{ Å}^3$, consistent with those previously reported for polycrystalline samples at room temperature. ¹⁷ The lattice parameters of Yb₁₄MgSb₁₁ refine to a = 16.623(1) Å, c = 22.259(1) Å, and V = 6150.9(8) Å³, slightly larger than what has previously been reported in both single crystals and polycrystalline samples which range from V = 6128(1) -6147(1) Å³. ^{18,31,48,49} In both cases the high purity of the sample is immediately evident and there is no indication of the presence of Yb₁₁Sb₁₀ or residual Yb₄Sb₃. However, a small Yb₂O₃ impurity was observed (1.08(6) wt% for Mn and 1.16(3) wt% for Mg) in both samples of $Yb_{14}MSb_{11}$ (M =Mg, Mn). The absence of Yb₁₁Sb₁₀ in either sample supports the hypothesis that Yb₁₄MSb₁₁ is slightly Yb deficient. Because these reactions are performed using oxide-free reagents (SI, Figures S1-5) in low oxygen atmospheres (< 0.5 ppm O_2), the source of the oxygen is likely from an external source. Oxygen has been shown to strongly chemisorb to the surface of graphite, 50-53 and therefore could come from the graphite die during the SPS processing. These C-O species do not desorb until temperatures above 1253 K,⁵² but unreacted Yb could react with these species to form Yb₂O₃ at temperatures below that, much like in the Nb₂O₅ case.

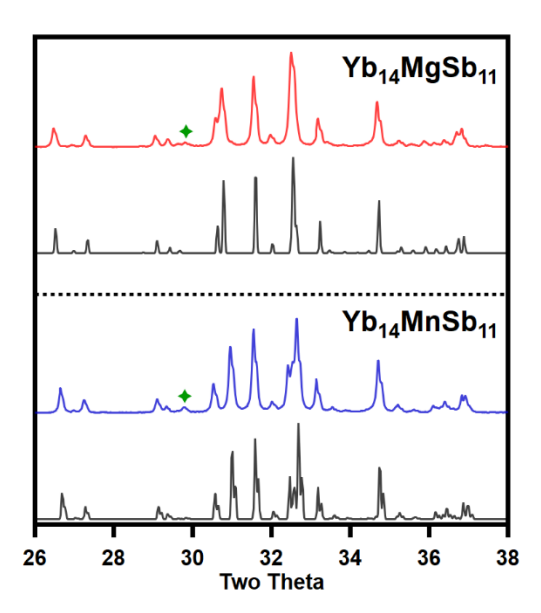


Figure 8. The PXRD patterns of Yb₁₄MgSb₁₁ (top) and Yb₁₄MnSb₁₁ (bottom) synthesized from Yb₄Sb₃, YbH₂, and Mg₃Sb₂ or MnSb. The patterns in black are references patterns calculated from the single crystal CIFs provided by Hu et al. and Brown et al. respectively. ^{18,44} The green star marks the most intense reflection from the Yb₂O₃ impurity.

In the reaction employing the binary phase Yb₁₁Sb₁₀ to form Yb₁₄MnSb₁₁, Yb₂O₃, Yb₁₁Sb₁₀, an Yb-rich phase and an Yb-deficient phase were identified by PXRD as the impurities. A Mn containing phase is also required to balance the reaction, but the amount would be too small to be detectable. This is also observed when making Yb₁₄MgSb₁₁ from Yb₁₁Sb₁₀ (SI, Figure S7). This is attributed to inhomogeneities of the starting reagents in the reaction mixture. However, in the reactions to form Yb₁₄MnSb₁₁ and Yb₁₄MgSb₁₁ from Yb₄Sb₃, only Yb₂O₃ is present among the final products, with a notable lack of Yb₁₁Sb₁₀ or other Yb-deficient Sb containing phases to balance the reaction. This suggests that the Yb₁₄MnSb₁₁ phase is Yb deficient as the stoichiometric reaction leaves unconsumed Yb, but apparently without accompanying Sb.

<u>Yb_{14-x}MnSb₁₁</u> Defect Study. To investigate the possibility that Yb₁₄MSb₁₁ phases are inherently Yb deficient, samples of Yb_{14-x}MnSb₁₁ were prepared employing YbH₂, MnSb, and Yb₄Sb₃ as binary precursors. The Yb content of the reaction was adjusted by changing equation 3 to be equal to the desired Yb content and then the 3-variable system of equations was re-solved based off the purity of the Yb₄Sb₃ being used for that reaction. Figure 9 a) shows the PXRD patterns of Yb_{14-x}MnSb₁₁ (x = 0, 0.02, 0.05) in comparison to the calculated pattern shown in black. All three samples show very high purity Yb₁₄MnSb₁₁. The pattern at the top of the plot is on stoichiometry for Yb, and those below that have systematically reduced Yb content. The powder diffraction pattern of the x = 0 sample refines with a 1.08(6) wt% Yb₂O₃ impurity present. As the Yb content of the reaction was reduced to 13.98 (x = 0.02), the refined oxide impurity in the PXRD pattern reduced to 0.76(6) wt%. At 13.95 (x = 0.05), the oxide impurity can no longer be refined. At 13.92 (x = 0.08) reflections from the Yb deficient phase, Yb₁₁Sb₁₀, are identified (SI, Figure S8). Figure 9 b) shows the highest intensity peak of Yb₂O₃ observed in these patterns. As the Yb content of the reaction is reduced, the intensity of this peak decreases until only the intensity of a peak related

to the Yb₁₄MnSb₁₁ phase is present. The apparent oxide impurity was systematically reduced through reduction of Yb content within the reaction. This further supports the hypothesis that the Yb₂O₃ observed in these reactions forms due to Yb-richness, either locally or overall. The systematic reduction in Yb content was further confirmed through energy dispersive spectroscopy (SI, Figures S9 - S12). Although the lattice parameters of the main Yb_{14-x}MnSb₁₁ phase (a = 16.6293(9) Å, c = 22.0458(9) Å, V = 6096.5(4) Å³) do not change, it is likely there are minor differences in defects within the samples. It has been shown in other materials that synthesis in a region of apparent elemental richness can influence the defects present in the main phase.^{54–56} A summary of the reactions and their products can be found in table 1.

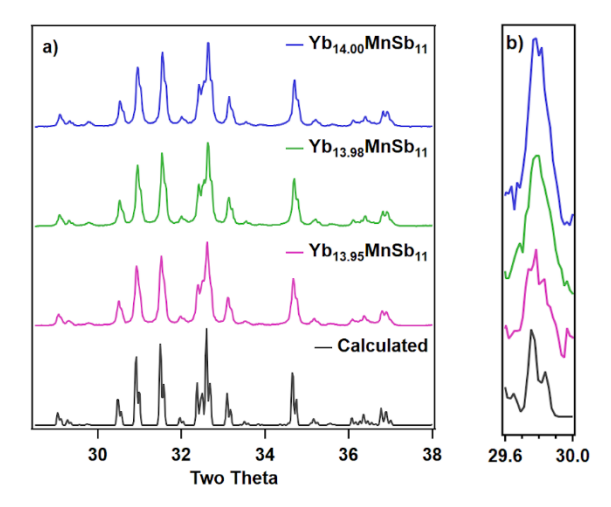


Figure 9. The a) powder x-ray diffraction patterns of $Yb_{14-x}MnSb_{11}$ with Yb content as indicated by the stoichiometry. The bottom pattern is a calculated diffraction pattern from the single crystal CIF. The enlarged 2θ region b) shows the most intense peak partially attributed to Yb_2O_3 . As Yb is reduced, this peak lowers in intensity until it matches the reference in black.

Table 1. A Summary of the Reactions to form $Yb_{14}MSb_{11}$ (M = Mg, Mn) from the Binaries and their Products from Rietveld Refinements

Reaction	Product	GoF, Rp, wRp
Yb ₁₄ MgSb ₁₁ from Yb ₁₁ Sb ₁₀	91.38(14) wt% Yb ₁₄ MgSb ₁₁ , 7.05(14) wt% Yb ₁₁ Sb ₁₀ , 1.56(6)	1.61, 7.18, 9.49
Yb ₁₄ MnSb ₁₁ from Yb ₁₁ Sb ₁₀	wt% Yb ₂ O ₃ 96.29(13) wt% Yb ₁₄ MnSb ₁₁ , 1.90(12) wt% Yb ₁₁ Sb ₁₀ , 1.81(5) wt% Yb ₂ O ₃	1.67, 6.94, 9.14
Yb ₁₄ MgSb ₁₁ from Yb ₄ Sb ₃	98.84(3) wt% Yb ₁₄ MgSb ₁₁ , 1.16(3) wt% Yb ₂ O ₃	1.64, 7.01, 9.56
Yb ₁₄ MnSb ₁₁ from Yb ₄ Sb ₃	98.98(5) wt% Yb ₁₄ MnSb ₁₁ , 1.08(6) wt% Yb ₂ O ₃	1.62, 6.61, 9.06
Yb _{13.98} MnSb ₁₁ from Yb ₄ Sb ₃	99.24(4) wt% Yb ₁₄ MnSb ₁₁ , 0.76(6) wt% Yb ₂ O ₃	1.54, 6.52, 8.71
Yb _{13.95} MnSb ₁₁ from Yb ₄ Sb ₃	100.00 wt% Yb ₁₄ MnSb ₁₁	1.56, 6.76, 9.21

Thermal Conductivity and Electrical Transport of Yb₁₄MgSb₁₁ and Yb_{14-x}MnSb₁₁. The thermal conductivity of the stoichiometric samples, Yb₁₄MgSb₁₁ and Yb₁₄MnSb₁₁, are shown in Figure 10 a). The Yb₁₄MgSb₁₁ sample shows a lower thermal conductivity compared with the Mn analog across the entire temperature range. Although the thermal conductivity is higher than what was previously reported for Yb₁₄MgSb₁₁,^{18,31} it can be attributed to differences in the electronic contribution. The thermal conductivity of the stoichiometric sample of Yb₁₄MnSb₁₁ is comparable to that previously reported.¹⁷ The "S-shaped" thermal conductivity seen here in both cases is indicative of the multiband transport which has been previously identified in these materials.⁴⁸

The Yb deficient series, Yb_{14-x}MnSb₁₁ (x = 0.02, 0.05) are also provided in Figure 9a. Yb_{13.98}MnSb₁₁ (x = 0.02) shows a nearly identical thermal conductivity to the stoichiometric compound until the highest temperatures which is shown in the inset. At 1073 K, the data deviates with a thermal conductivity of 7.70 mW cm⁻¹ K⁻¹ and provides a consistently higher thermal conductivity, reaching a maximum of 8.71 mW cm⁻¹ K⁻¹ at 1273 K. The more deficient structure, Yb_{13.95}MnSb₁₁ (x = 0.05) shows an overall lower thermal conductivity, starting at 7.78 mW cm⁻¹ K⁻¹ at 327 K, increasing to 8.39 mW cm⁻¹ K⁻¹ at 574 K and then decreasing to a minimum of 7.46 mW cm⁻¹ K⁻¹ at 1073 K. Following the typical temperature dependence for this structure type, the thermal conductivity above 1073 K increases to 8.56 mW cm⁻¹ K⁻¹ at 1273 K. The thermal conductivity of the x = 0.05 sample fits closely what has been reported for single crystals samples.^{17,44} What is most noticeable in this series is the distinctly different slope of the stoichiometric sample after the onset of bipolar conductance in comparison to both Yb deficient samples, shown in the inset of Figure 9a. This suggests that a slight excess in Yb may play a role in the manipulation of transport properties at the highest temperatures.

The electrical resistivity as a function of temperature for all samples are shown in Figure 10 b). Consistent with the higher thermal conductivity, Yb₁₄MgSb₁₁ exhibits a lower electrical resistivity than previously published. 18,31 This is likely due to the reduction of Mg employed compared to previously published reactions (typically 20% excess) thereby reducing unreacted Mg at grain boundaries, which has previously been shown to have negative effects on the electrical resistivity. 31 The electrical resistivity of Yb₁₄MgSb₁₁ is 2.35 mΩ·cm at 294 K and increases to a maximum of 7.41 mΩ·cm at 1250 K. The Yb_{14-x}MnSb₁₁ series of samples all start at the same approximate value at room temperature. The resistivity of Yb_{14-x}MnSb₁₁ series at 294 K are 1.92 $m\Omega \cdot cm$, 1.91 $m\Omega \cdot cm$, and 2.04 $m\Omega \cdot cm$, for x = 0.00, 0.02, 0.05, respectively. As temperature increases, x = 0.00 shows the lowest resistivity, with x = 0.02 above that, and x = 0.05 the highest. By 800 K this ordering is noticeable with the resistivities of 3.78 m Ω ·cm, 3.92 m Ω ·cm and 4.19 $m\Omega \cdot cm$, for the x = 0.00, 0.02, and 0.05, respectively. At 1175 K, the resistivities of the two Ybdeficient samples begin to bend over due to bipolar conduction. Notably, the x = 0.00 shows a less drastic change in slope and the resistivity continues upwards until the final temperature is reached. The high temperature behavior can be seen in the enlarged view shown as an inset in Figure 9b. The electrical resistivity of all samples within the Yb_{14-x}MnSb₁₁ series fit well with what has previously been reported for samples of this material, with those having the highest performance showing the same high temperature behavior as the stoichiometric (x = 0.00) sample. ^{17,44}

The Hall carrier concentration versus temperature is shown in Figure 10 c). The carrier concentration of Yb₁₄MgSb₁₁ starts below that of the Mn analog at 6.74 x 10²⁰ h⁺ cm⁻³ at 294 K, higher than what has previously been reported (5.37 x 10²⁰ h⁺ cm⁻³).³¹ The carrier concertation stays relatively level with increasing temperature until around 900 K. At that point, there is an increase in carrier concentration to a maximum of 4.56 x 10²¹ h⁺ cm⁻³ at 1250 K. The increase in carrier concentration at the highest temperature can be attributed to the onset of bipolar conductance. For the Yb_{14-x}MnSb₁₁ series, the carrier concentration at 294 K begins at 1.48 x 10²¹ h^+ cm⁻³, 1.15 x 10²¹ h^+ cm⁻³, and 1.09 x 10²¹ h^+ cm⁻³, for x = 0.00, 0.02, 0.05, respectively. All three samples converge to approximately 9 x 10²⁰ h⁺ cm⁻³ by 400 K. The carrier concentrations of the three samples are in close agreement until 700 K, where they begin to deviate and by 800 K the difference is significant. Yb₁₄MnSb₁₁ shows a higher carrier concentration of 1.14 x 10²¹ h⁺ cm⁻³ at 807 K in comparison to $Yb_{13.98}MnSb_{11}$ (7.19 x $10^{20}\ h^+$ cm⁻³) and $Yb_{13.95}MnSb_{11}$ (8.04 x $10^{20}\ h^+$ cm⁻³). This trend holds true as the temperature increases with x = 0.00 having the highest carrier concentration, x = 0.05 having a lower carrier concentration, and x = 0.02 being close to that, but lower. Around 1000 K there is a noticeable increase in the carrier concentrations of all three samples which is attributed to the onset of bipolar conduction. The samples of Yb_{14-x}MnSb₁₁ all have the same carrier concentration as what has previously been reported of 9 x 10²⁰ h⁺ cm⁻³ at 400 K.¹⁷ The noticeable difference in temperature dependent carrier concentration seen in the Yb₁₄MnSb₁₁ in comparison to the deficient samples may be a result of the apparent Yb richness and its influence on defects within the main phase.

The Hall mobility (Figure 10 d)) of Yb₁₄MgSb₁₁ starts at 4.0 cm² V⁻¹ s⁻¹ at 294 K, then increases to 4.48 cm² V⁻¹ s⁻¹ at 352 K. After that, the mobility steadily decreases to 0.175 cm² V⁻¹ s⁻¹ at 1250 K. The Hall mobility of Yb₁₄MnSb₁₁ starts at 2.20 cm² V⁻¹ s⁻¹ at room temperature. In comparison, the two deficient samples both show higher room temperature carrier mobilities of 2.84 cm² V⁻¹ s⁻¹ and 2.82 cm² V⁻¹ s⁻¹ for x = 0.02, 0.05, respectively. The mobility of these samples remains relatively unchanged until 550 K where there is a drastic decrease in the carrier mobility of all samples as they trend downwards towards 0.5 cm² V⁻¹ s⁻¹ at 1273 K. The trends in mobility agree with those seen in the higher temperature region of the carrier concentration. The sample with the highest carrier concentration (x = 0.00) has the lowest mobility, and that with the lowest carrier concentration (x = 0.02) has the highest. The carrier mobilities of Yb₁₄MgSb₁₁ are slightly lower than what was previously reported which is expected with the higher carrier concentrations seen in this sample (4.48 vs 4.70 cm² V⁻¹ s⁻¹).³¹ The carrier mobilities of the Yb_{14-x}MnSb₁₁ series are comparable to what has previously been reported for single crystal and polycrystalline samples with the two deficient samples showing mobilities closer to that of the single crystal results.^{57,58}

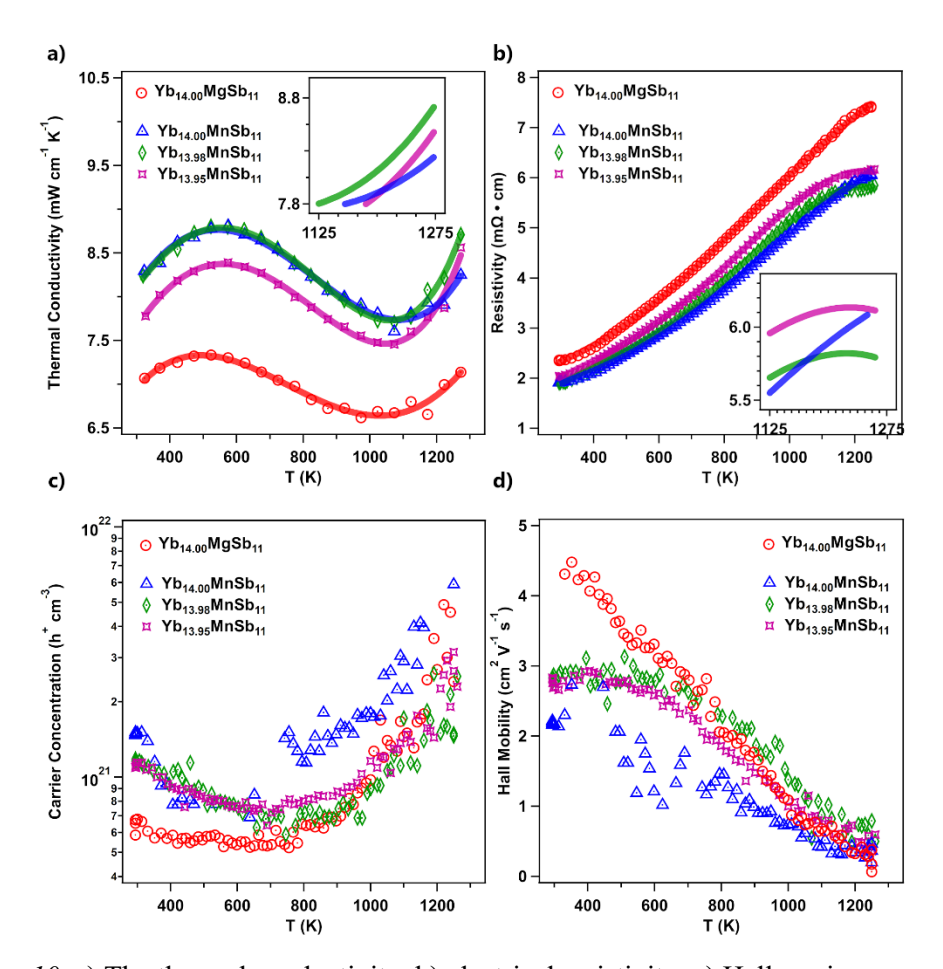


Figure 10. a) The thermal conductivity, b) electrical resistivity, c) Hall carrier concentration and d) carrier mobility as a function of temperature of $Yb_{14}MgSb_{11}$ and the $Yb_{14-x}MnSb_{11}$ series. Markers are the experimental data points and lines are polynomial fits employed for calculation of zT.

Seebeck Coefficients. Figure 11 a) shows the Seebeck coefficients as a function of temperature for all samples. The Mg analog shows a systematically higher Seebeck coefficient which steadily increases with temperature, reaching a maximum of 231.49 µV K⁻¹ at 1181 K before decreasing due to the onset of bipolar conduction. ^{18,31,48} The Yb_{14-x}MnSb₁₁ stoichiometric sample begins at a value of 44.83 μV K⁻¹ at 313 K and steadily increases to a maximum of 221.29 μV K⁻¹ at 1250 K, after which there is a bend over due to the onset of bipolar conduction. The x = 0.02 sample, Yb_{13.98}MnSb₁₁, shows a higher Seebeck coefficient of 48 μV K⁻¹ at 312 K, but as temperature increases, it reaches a lower peak of 214.65 µV K⁻¹ at 1212 K after which the Seebeck coefficient bends over. The most Yb deficient x = 0.05 sample, Yb_{13.95}MnSb₁₁, starts between the other two samples at 46.74 µV K⁻¹ at 321 K. As temperature increases, the Seebeck coefficient of this sample also increases, but only reaches a maximum of 212.50 µV K⁻¹ at 1214 K. After that point, the data bends over due to bipolar conduction. The inset in Figure 10a shows the Seebeck coefficients at the highest temperatures. In this temperature range, the ordering of the Seebeck coefficients follows the Yb deficiency with x = 0.00 having the highest Seebeck coefficient and x = 0.05 having the lowest. The maximum Seebeck coefficient of Yb₁₄MgSb₁₁ is comparable to the 232 µV K⁻¹ previously reported.³¹ The values for Yb_{14-x}MnSb₁₁ agree with what has previously been reported, with the stoichiometric sample having maximum values that match the highest efficiency samples.¹⁷ Using the Goldsmid-Sharp method for estimating band gap, the band gaps of Yb₁₄MgSb₁₁ and Yb₁₄MnSb₁₁ were both estimated to be about 0.55 eV.⁵⁹ This is close to what has been previously calculated from experimental and computational methods.^{17,18,31,48,55}

The Seebeck coefficients of the stoichiometric Yb14MgSb11 and Yb14MnSb11 were also measured using a commercially available Linseis LSR-3 employing an off axis 4-probe orientation (SI, Figure S14). This measurement configuration is much more accessible to a wider range of laboratories and commercial settings. Although this method is employed by many research laboratories, it is known that the 4-probe method provides systematically larger Seebeck coefficients due to a phenomena known as the "cold finger" effect. 25,60 There is a tendency to underestimate the actual thermal gradient, and in turn overestimate the Seebeck coefficient $(\Delta V/\Delta T)$ due to heat flow being directed into the probes and away from the surface of the sample. The room temperature Seebeck coefficients of both samples are comparable to those measured by the 2-probe method. This trend holds true until 700 K. At that point, both 4 probe measurements begin to show systematically larger Seebeck coefficients which deviate further with temperature from the 2-probe measurements. By 900 K the sample of Yb₁₄MgSb₁₁ has a Seebeck coefficient of 213 µV K⁻¹ versus 192 µV K⁻¹ for the 4-probe versus the 2-probe method. The stoichiometric sample of Yb₁₄MnSb₁₁ shows similar deviations, reaching 190 uV K⁻¹ at 900 K by the 4-probe method and 175 µV K⁻¹ by the 2-probe method. The sample of Yb₁₄MgSb₁₁ provides a maximum of 276 µV K⁻¹ at 1272 K and Yb₁₄MnSb₁₁ reaches 256 µV K⁻¹ at 1225 K. These Seebeck coefficients are 19% and 16% larger than the maximums measured by the 2-probe method.

A Pisarenko plot of the Yb_{14-x}MnSb₁₁ series (Figure 11 b)) at 900 K shows the variation in effective mass between the two non-stoichiometric samples and the stoichiometric Yb₁₄MnSb₁₁ at temperatures above where the difference in carrier concentration was observed. The x = 0.00 sample in the Ybn_{14-x}MnSb₁₁ series was calculated to have an effective mass of 5.24 m₀ whereas x = 0.02 and 0.05 showed 3.05 m₀ and 3.42 m₀, respectively, at 900 K. There is the clear trend of increasing effective mass with increasing carrier concentration. This is consistent with the electronic structure and modeling of the multiband transport of Yb₁₄MnSb₁₁ and the Yb₁₄Mg_{1-x}Al_xSb₁₁ series.⁴⁸ As carrier concentration is increased to 1 x 10²¹ h⁺ cm⁻³ and beyond, the Fermi level is pushed deeper into the valence band. As the Fermi-Dirac distribution and in turn selection functions broaden, this deeper Fermi level allows for more selection from a pocket of heavy, degenerate bands located between N-P before the onset of bipolar conduction.

<u>Unitless Thermoelectric Figure of Merit, zT.</u> The overall thermal to electric conversion performance of thermoelectric materials is judged by the unitless thermoelectric figure of merit, $zT = S^2T/\rho\kappa$, where S is the Seebeck coefficient, T is the absolute temperature, ρ is the electrical resistivity, and κ is the thermal conductivity. Figure 11 c) shows the calculated zT for Yb₁₄MgSb₁₁ and Yb_{14-x}MnSb₁₁. The sample of Yb₁₄MgSb₁₁ reaches a peak zT of 1.28 at 1175 K. This is slightly higher than the previous best for this material of 1.26 and brings the Mg analog even closer to the highest reported values for Yb₁₄MnSb₁₁ (1.35 at 1273 K).^{17,31} Although peak efficiencies are lower, the average zT of this sample from 875 to 1275K is 1.15, which is slightly higher than the one of the best sample of Yb₁₄MnSb₁₁ (1.07).¹⁷ This is important when considering a material for implementation into a thermoelectric generator where the individual legs operate within a large

temperature range. The calculated figure of merit for Yb_{14-x}MnSb₁₁ starts at a maximum of 1.24 at 1275 K for x = 0.00. The Yb-deficient samples both show lower peak zT of 1.16 and 1.12 for x =0.02 and 0.05, respectively, at 1225 K. The efficiencies calculated for the stoichiometric sample of Yb_{14-x}MnSb₁₁ match the best previously reported values for polycrystalline samples measured by the same method and the sample which showed no impurities by PXRD (x = 0.05) shows performances closer to what has been previously reported for single crystal samples. 17,44 The figure of merit was also calculated using the Seebeck coefficients and electrical resistivities measured by the off axis 4-probe method (SI, Figure S13-S15). Yb₁₄MgSb₁₁ has a calculated zT of 1.83 at 1275 K and Yb₁₄MnSb₁₁ provides 1.71 at 1275 K. Both of these are the highest reported zT for their respective phases and are competitive with some of the highest reported efficiencies for any high temperature materials measured by this method with the peak efficiencies coming at a higher temperature range than that of high performing half Heusler phases. ^{61–69} It is likely the efficiencies measured by the 4-probe method are somewhat exaggerated due to the cold finer effect, but these values allow for more direct comparison to other materials measured by the 4-probe method. A systematic study of Yb_{14-x}MnSb₁₁ has shown that synthesis in a region of apparent elemental excess can lead to improved properties. It is known that the impurities found at grain boundaries in polycrystalline samples can influence the minor defects present in the main phase. 54–56,70 These results suggest further exploration of this phase space through phase boundary mapping could lead to the realization of further improved properties and a better understanding of defects and the effects of impurities within these complex systems. 54,56,70,71

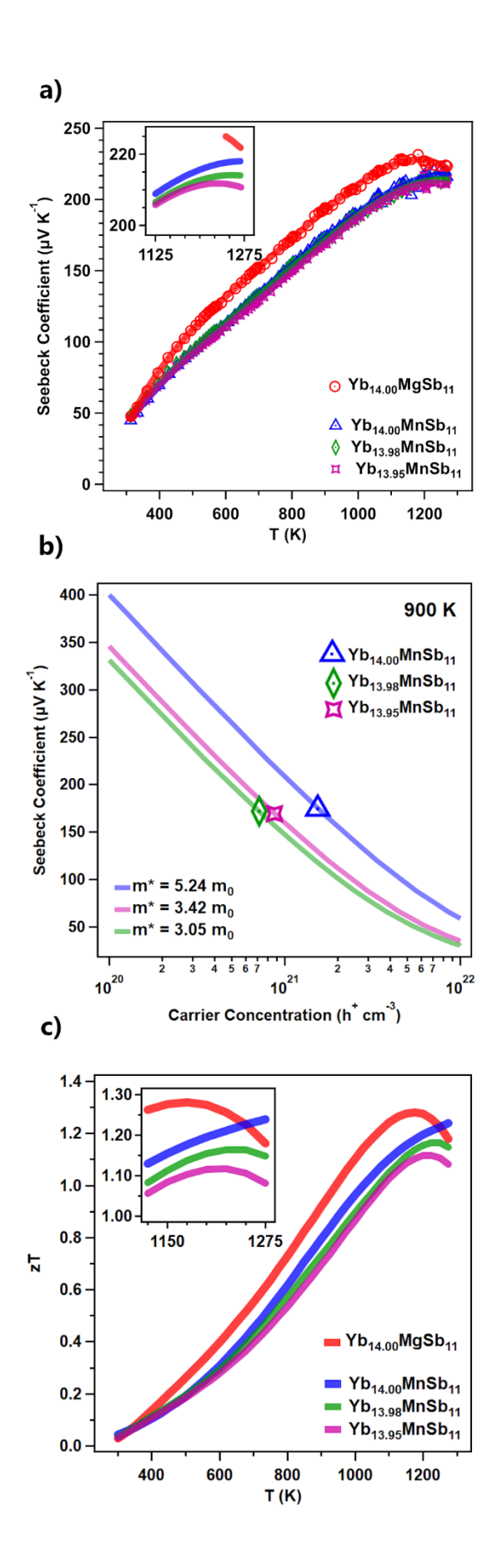


Figure 11. a) The Seebeck coefficient of $Yb_{14}MgSb_{11}$ and the $Yb_{14-x}MnSb_{11}$ series. b) A Pisarenko plot of the $Yb_{14-x}MnSb_{11}$ series at 900 K. c) The unitless thermoelectric figure of merit (zT) for $Yb_{14}MgSb_{11}$ and the $Yb_{14-x}MnSb_{11}$ series. Markers represent experimental data and lines provide calculated values.

Conclusion

The advancement of thermoelectric materials depends on the quality of materials and in terms of device fabrication, high reproducibility and fidelity in preparing samples of a particular composition with optimal properties. While Zintl phases have found many successes in thermoelectrics, compositions of the stoichiometry Yb₁₄MSb₁₁ and other complex structures are difficult to prepare for reasons articulated in the beginning of the discussion. A better understanding of the reaction paths leading to the formation of $Yb_{14}MSb_{11}$ (M = Al, Mn) was obtained through thorough quenching studies paired with PXRD. These studies revealed Yb₁₁Sb₁₀ and Yb₄Sb₃ as binary intermediates which were investigated for use as precursors in reactions with with YbH₂ and MnSb or Mg₃Sb₂. An improved synthetic route is shown to allow for efficient synthesis of stoichiometric and extremely high purity products. Through this synthesis a sample of Yb₁₄MgSb₁₁ was produced which exhibited material leading efficiencies of zT = 1.28 at 1175 K. The slight improvement to overall zT increased the zT_{avg} of $Yb_{14}MgSb_{11}$ in the temperature window 875 to 1275K from 1.10 to 1.15, making this phase competitive with Yb₁₄MnSb₁₁ $(1.07)^{17,31,72}$ The increase in average zT is important when considering these materials for incorporation into high temperature thermoelectric generators, such as a Radioisotope Thermoelectric Generator (RTG). The impact of experimental method in acquiring the Seebeck coefficient was also investigated and showed that while the commercial 4-probe experimental setup provides reliable electrical resistivity, the Seebeck coefficients are exaggerated due to a coldfinger effect at high temperatures. However, instruments using this orientation are commercially available and accessible to a wider range of users making it a useful tool in the study of thermoelectric materials. The method used in the measurement of high temperature Seebeck coefficients should always be considered when comparing data, and the 4-probe measurements presented herein allow for more direct comparison to other materials which have been measured by this method.

This synthetic route provides a high degree of stoichiometric control which was used to adjust the Yb content of reactions. The employment of binary phases was used to investigate the source of the small Yb₂O₃ impurity found for Yb₁₄MSb₁₁. Based on the reduction of Yb₂O₃ in the final samples, the actual composition is slightly Yb deficient with the stoichiometry of Yb_{13.95}MnSb₁₁. Through the reduction of the apparent oxide impurity, the thermoelectric properties of Yb_{14-x}MnSb₁₁ resulted in systematically lower zT. This suggests that the excess Yb plays a role in obtaining a composition with good high temperature transport properties in the case of the M = M analog and warrants further exploration through phase boundary mapping. Through this synthetic approach, a high degree of stoichiometric control is obtained, which allows for accurate mapping of the phase space and provides a roadmap for the realization of optimal compositions for high thermoelectric performance in these phases. In addition to the Yb₁₄MnSb₁₁ region of phase

space, this binary addition approach could be applied to explore other difficult ternary systems with a high degree of precision.

Associated Content

<u>Supporting Information.</u> Additional X-ray diffraction patterns, scanning electron micrographs, energy dispersive spectroscopy results, 4-probe thermoelectric measurements, and heating/cooling curves from thermoelectric measurements can be found in the Supporting Information (PDF). This material is free of charge and available at http://pubs.acs.org.

Acknowledgements

This work was supported by NSF DMR-2001156. The thermoelectric measurements were performed in part at the Jet Propulsion Laboratory, California Institute of Technology under contract with the National Aeronautics and Space Administration. G. Cerretti's research at the Jet Propulsion Laboratory was supported by an appointment to the NASA Postdoctoral Program, administered by Universities Space Research Association under contract with NASA. The SEM EDX characterization was performed in the Advanced Materials Characterization and Technology (AMCaT) Laboratory at University of California, Davis supported by NSF DMR-1725618.

References

- (1) Klein, M. T.; Neurock, M.; Broadbelt, L.; Foley, H. C. Reaction Pathway Analysis. Global Molecular and Mechanistic Perspectives. *ACS Symp. Ser.* **1993**, *517*, 290–315.
- (2) Carino, A.; Testino, A.; Andalibi, M. R.; Pilger, F.; Bowen, P.; Ludwig, C. Thermodynamic-Kinetic Precipitation Modeling. A Case Study: The Amorphous Calcium Carbonate (ACC) Precipitation Pathway Unravelled. *Cryst. Growth Des.* **2017**, *17* (4), 2006–2015. https://doi.org/10.1021/acs.cgd.7b00006.
- (3) Edwards, J. O. Mechanisms of Inorganic Reactions. *Inorg. Chem.* **1966**, *5* (4), 702–702. https://doi.org/10.1021/ic50038a051.
- (4) Lin, Z.; Hall, M. B. Theoretical Studies of Inorganic and Organometallic Reaction Mechanisms. 5. Substitution Reactions of 17- and 18-Electron Transition-Metal Hexacarbonyl Complexes. *Inorg. Chem.* **1992**, *31* (13), 2791–2797. https://doi.org/10.1021/ic00039a024.
- (5) Davy, R. D.; Hall, M. B. Theoretical Studies of Inorganic and Organometallic Reaction Mechanisms. 1. Cis Labilization in Carbonyl Substitution Reactions of Hexacoordinate Chromium(0) and Manganese(I) Pentacarbonyl Complexes. *Inorg. Chem.* **1989**, *28* (18), 3524–3529. https://doi.org/10.1021/ic00317a026.
- (6) Lin, Z.; Hall, M. B. Theoretical Studies of Inorganic and Organometallic Reaction Mechanisms. 2. The Trans Effect in Square-Planar Platinum(II) and Rhodium(I) Substitution Reactions. *Inorg. Chem.* **1991**, *30* (4), 646–651. https://doi.org/10.1021/ic00004a011.
- (7) Pati, S.; Rayi, S.; Namboothiri, I. N. N. Stereoselective Synthesis of Tri- and

- Tetrasubstituted Olefins via 1,6-Additions of Diazo Compounds and Their Precursors to p -Quinone Methides. *ACS Org. Inorg. Au* **2021**, *I* (2), 51–59. https://doi.org/10.1021/acsorginorgau.1c00012.
- (8) Arora, A.; Teegardin, K. A.; Weaver, J. D. Reductive Alkylation of 2-Bromoazoles via Photoinduced Electron Transfer: A Versatile Strategy to Csp²-Csp³ Coupled Products. *Org. Lett.* **2015**, *17* (15), 3722–3725. https://doi.org/10.1021/acs.orglett.5b01711.
- (9) Kovnir, K. Predictive Synthesis. *Chem. Mater.* **2021**, *33* (13), 4835–4841. https://doi.org/10.1021/acs.chemmater.1c01484.
- (10) Ogata, A. F.; Mirabello, G.; Rakowski, A. M.; Patterson, J. P. Revealing Nonclassical Nucleation Pathways Using Cryogenic Electron Microscopy. In *ACS Symposium Series*; UTC, 2020; Vol. 1358, pp 147–200. https://doi.org/10.1021/bk-2020-1358.ch007.
- (11) Weiland, A.; Frith, M. G.; Lapidus, S. H.; Chan, J. Y. In Situ Methods for Metal-Flux Synthesis in Inert Environments. *Chem. Mater.* **2021**, *33* (19), 7657–7664. https://doi.org/10.1021/acs.chemmater.1c02413.
- (12) Paik, J. A.; Brandon, E.; Caillat, T.; Ewell, R.; Fleurial, J. P. Life Testing of Yb₁₄MnSb₁₁ for High Performance Thermoelectric Couples. In *Nuclear and Emerging Technologies* for Space 2011, NETS-2011; Albuquerque, NM, 2011; pp 616–622.
- (13) Firdosy, S. A.; Chun-Yip Li, B.; Ravi, V. A.; Sakamoto, J.; Caillat, T.; Ewell, R. C.; Brandon, E. Metallization for Yb₁₄MnSb₁₁-Based Thermoelectric Materials NPO-46670. *NASA Tech Briefs* **2011**, *35* (8), 34–36.
- (14) Lee, K.; Puleo, B.; Setlock, J. Sublimation Protection Coatings for Thermoelectric Materials for Space Power Applications https://ntrs.nasa.gov/citations/20190032204 (accessed Oct 29, 2021).
- (15) Ravi, V.; Firdosy, S.; Caillat, T.; Brandon, E.; Van Der Walde, K.; Maricic, L.; Sayir, A. Thermal Expansion Studies of Selected High-Temperature Thermoelectric Materials. *J. Electron. Mater.* **2009**, *38* (7), 1433–1442. https://doi.org/10.1007/S11664-009-0734-2.
- (16) Brandon, E.; Caillat, T.; Fleurial, J.-P.; Ewell, R.; Li, B.; Firdosy, S.; Paik, J.-A.; Nakatsukasa, G.; Huang, C.-K.; Nesmith, B.; et al. Development of New High Temperature Power Generating Couples for the Advanced Thermoelectric Converter (ATEC). In 40th International Conference on Environmental Systems; American Institute of Aeronautics and Astronautics: Reston, Virigina, 2010; pp 1–7. https://doi.org/10.2514/6.2010-7004.
- (17) Grebenkemper, J. H.; Hu, Y.; Barrett, D.; Gogna, P.; Huang, C.-K.; Bux, S. K.; Kauzlarich, S. M. High Temperature Thermoelectric Properties of Yb₁₄MnSb₁₁ Prepared from Reaction of MnSb with the Elements. *Chem. Mater.* **2015**, *27* (16), 5791–5798. https://doi.org/10.1021/acs.chemmater.5b02446.
- (18) Hu, Y.; Wang, J.; Kawamura, A.; Kovnir, K.; Kauzlarich, S. M. Yb₁₄MgSb₁₁ and Ca₁₄MgSb₁₁ New Mg-Containing Zintl Compounds and Their Structures, Bonding, and Thermoelectric Properties. *Chem. Mater.* **2015**, *27* (1), 343–351. https://doi.org/10.1021/cm504059t.

- (19) Liu, K.-F.; Xia, S.-Q. Recent Progresses on Thermoelectric Zintl Phases: Structures, Materials and Optimization. *J. Solid State Chem.* **2019**, *270* (November 2018), 252–264. https://doi.org/10.1016/j.jssc.2018.11.030.
- (20) Kauzlarich, S. M.; Devlin, K. P.; Perez, C. J. Zintl Phases for Thermoelectric Applications. In *Thermoelectric Energy Conversion*; 2021; pp 157–182. https://doi.org/10.1016/b978-0-12-818535-3.00004-9.
- (21) Kauzlarich, S. M.; Zevalkink, A.; Toberer, E.; Snyder, G. J. Zintl Phases: Recent Developments in Thermoelectrics and Future Outlook. In *RSC Energy and Environment Series*; 2017; Vol. 2017-Janua, pp 1–26. https://doi.org/10.1039/9781782624042-00001.
- (22) Kauzlarich, S. M.; Brown, S. R.; Jeffrey Snyder, G. Zintl Phases for Thermoelectric Devices. *Dalt. Trans.* **2007**, No. 21, 2099. https://doi.org/10.1039/b702266b.
- (23) Fleurial, J.; Caillat, T.; Nesmith, B. J.; Ewell, R. C.; Woerner, D. F.; Carr, G. C.; Jones, L. E. Thermoelectrics: From Space Power Systems to Terrestrial Waste Heat Recovery Applications. In *2nd Thermoelectrics Applications Workshop*; 2011.
- (24) Mahan, G. D. Introduction to Thermoelectrics. *APL Mater.* **2016**, *4* (10), 104806. https://doi.org/10.1063/1.4954055.
- (25) Zevalkink, A.; Smiadak, D. M.; Blackburn, J. L.; Ferguson, A. J.; Chabinyc, M. L.; Delaire, O.; Wang, J.; Kovnir, K.; Martin, J.; Schelhas, L. T.; et al. A Practical Field Guide to Thermoelectrics: Fundamentals, Synthesis, and Characterization. *Appl. Phys. Rev.* **2018**, *5* (2), 021303. https://doi.org/10.1063/1.5021094.
- (26) Urban, J. J.; Menon, A. K.; Tian, Z.; Jain, A.; Hippalgaonkar, K. New Horizons in Thermoelectric Materials: Correlated Electrons, Organic Transport, Machine Learning, and More. *J. Appl. Phys.* **2019**, *125* (18), 180902. https://doi.org/10.1063/1.5092525.
- (27) Kazem, N.; Kauzlarich, S. M. Thermoelectric Properties of Zintl Antimonides. In *Handbook on the Physics and Chemistry of Rare Earths*; Elsevier, 2016; Vol. 50, pp 177–208. https://doi.org/10.1016/bs.hpcre.2016.05.003.
- (28) Iversen, B. B. Breaking Thermoelectric Performance Limits. *Nature Materials*. October 2, 2021, pp 1309–1310. https://doi.org/10.1038/s41563-021-01065-5.
- (29) Petříček, V.; Dušek, M.; Palatinus, L. Crystallographic Computing System JANA2006: General Features. *Zeitschrift für Krist. Cryst. Mater.* **2014**, *229* (5), 345–352. https://doi.org/10.1515/zkri-2014-1737.
- (30) Devlin, K. P.; Grebenkemper, J. H.; Lee, K.; Cerretti, G.; Bux, S. K.; Kauzlarich, S. M. Enhancement of the Thermal Stability and Thermoelectric Properties of Yb₁₄MnSb₁₁ by Ce Substitution. *Chem. Mater.* **2020**, *32* (21), 9268–9276. https://doi.org/10.1021/acs.chemmater.0c03043.
- (31) Justl, A. P.; Cerretti, G.; Bux, S. K.; Kauzlarich, S. M. Hydride Assisted Synthesis of the High Temperature Thermoelectric Phase: Yb₁₄MgSb₁₁. *J. Appl. Phys.* **2019**, *126* (16), 165106. https://doi.org/10.1063/1.5117291.
- (32) Sui, F.; Bux, S. K.; Kauzlarich, S. M. Influence of YbP on the Thermoelectric Properties

- of N-Type P Doped Si₉₅Ge₅ Alloy. *J. Alloys Compd.* **2018**, *745*, 624–630. https://doi.org/10.1016/j.jallcom.2018.02.184.
- (33) Borup, K. A.; Zoltan, L. D.; Snyder, G. J.; Fleurial, J.-P.; Toberer, E. S.; Errico, M.; Iversen, B. B.; Nakatsukasa, G. Measurement of the Electrical Resistivity and Hall Coefficient at High Temperatures. *Rev. Sci. Instrum.* **2012**, *83* (12), 123902. https://doi.org/10.1063/1.4770124.
- (34) Wood, C.; Zoltan, D.; Stapfer, G. Measurement of Seebeck Coefficient Using a Light Pulse. *Rev. Sci. Instrum.* **1985**, *56* (5), 719–722. https://doi.org/10.1063/1.1138213.
- (35) James, S. L.; Adams, C. J.; Bolm, C.; Braga, D.; Collier, P.; Friščić, T.; Grepioni, F.; Harris, K. D. M.; Hyett, G.; Jones, W.; et al. Mechanochemistry: Opportunities for New and Cleaner Synthesis. *Chem. Soc. Rev.* **2012**, *41* (1), 413–447. https://doi.org/10.1039/C1CS15171A.
- (36) Baláž, P. *Mechanochemistry in Nanoscience and Minerals Engineering*; Springer Berlin Heidelberg: Berlin, Heidelberg, 2008. https://doi.org/10.1007/978-3-540-74855-7.
- (37) Mateti, S.; Mathesh, M.; Liu, Z.; Tao, T.; Ramireddy, T.; Glushenkov, A. M.; Yang, W.; Chen, Y. I. Mechanochemistry: A Force in Disguise and Conditional Effects towards Chemical Reactions. *This J. is Cite this Chem. Commun* **2021**, *57*, 1080. https://doi.org/10.1039/d0cc06581a.
- (38) Cordova, D. L. M.; Johnson, D. C. Synthesis of Metastable Inorganic Solids with Extended Structures. *ChemPhysChem* **2020**, *21* (13), 1345–1368. https://doi.org/10.1002/cphc.202000199.
- (39) Anderson, M. D.; Thompson, J. O.; Johnson, D. C. Avoiding Binary Compounds as Reaction Intermediates in Solid State Reactions. *Chem. Mater.* **2013**, *25* (20), 3996–4002. https://doi.org/10.1021/cm4019259.
- (40) Choffel, M. A.; Gannon, R. N.; Göhler, F.; Miller, A. M.; Medlin, D. L.; Seyller, T.; Johnson, D. C. Synthesis and Electrical Properties of a New Compound (BiSe)_{0.97}(Bi₂Se₃)_{1.26}(BiSe)_{0.97}(MoSe₂) Containing Metallic 1T-MoSe 2. *Chem. Mater.* **2021**, *33* (16), 6403–6411. https://doi.org/10.1021/acs.chemmater.1c01623.
- (41) Göhler, F.; Choffel, M. A.; Schmidt, C.; Zahn, D. R. T.; Johnson, D. C.; Seyller, T. Influence of Nanoarchitectures on Interlayer Interactions in Layered Bi–Mo–Se Heterostructures. *J. Phys. Chem. C* 2021, 125 (17), 9469–9478. https://doi.org/10.1021/acs.jpcc.1c01731.
- (42) Zalden, P.; Koch, C.; Paulsen, M.; Esters, M.; Johnson, D. C.; Wuttig, M.; Lindenberg, A. M.; Bensch, W. Acceleration of Crystallization Kinetics in Ge-Sb-Te-Based Phase-Change Materials by Substitution of Ge by Sn. *Adv. Funct. Mater.* **2021**, *31* (1), 2004803. https://doi.org/10.1002/adfm.202004803.
- (43) Vasilyeva, I.; Abdusalyamova, M.; Makhmudov, F.; Eshov, B.; Kauzlarich, S. Thermal Air-Oxidized Coating on Yb_{14-x}RE_xMnSb₁₁ Ceramics. *J. Therm. Anal. Calorim.* **2019**, *136* (2), 541–548. https://doi.org/10.1007/s10973-018-7659-z.
- (44) Brown, S. R.; Kauzlarich, S. M.; Gascoin, F.; Snyder, G. J. Yb₁₄MnSb₁₁: New High

- Efficiency Thermoelectric Material for Power Generation. *Chem. Mater.* **2006**, *18* (7), 1873–1877. https://doi.org/10.1021/cm060261t.
- (45) Cervantes, O. G.; Kuntz, J. D.; Gash, A. E.; Munir, Z. A. Activation Energy of Tantalum—Tungsten Oxide Thermite Reactions. *Combust. Flame* **2011**, *158* (1), 117–122. https://doi.org/10.1016/j.combustflame.2010.07.023.
- (46) Fan, R.-H.; Lü, H.-L.; Sun, K.-N.; Wang, W.-X.; Yi, X.-B. Kinetics of Thermite Reaction in Al-Fe₂O₃ System. *Thermochim. Acta* **2006**, *440* (2), 129–131. https://doi.org/10.1016/j.tca.2005.10.020.
- (47) Ahmadi-Binahri, A.; Adeli, M.; Aboutalebi, M. R.; Krasikov, S. Implementation of Thermite Reactions in the Production of Advanced Intermetallic-Matrix Composites: The Case of Nb₂O₅/Al Thermite Mixture. *Met. Mater. Int.* **2021**, No. 0123456789. https://doi.org/10.1007/s12540-021-01047-x.
- (48) Perez, C. J.; Wood, M.; Ricci, F.; Yu, G.; Vo, T.; Bux, S. K.; Hautier, G.; Rignanese, G.-M. M.; Snyder, G. J.; Kauzlarich, S. M. Discovery of Multivalley Fermi Surface Responsible for the High Thermoelectric Performance in Yb₁₄MnSb₁₁and Yb₁₄MgSb₁₁. *Sci. Adv.* **2021**, *7* (4), eabe9439. https://doi.org/10.1126/sciadv.abe9439.
- (49) Perez, C. J.; Qi, X.; Chen, Z.; Bux, S. K.; Chanakain, S.; Li, B.; Liu, K.; Dhall, R.; Bustillo, K. C.; Kauzlarich, S. M. Improved Power Factor and Mechanical Properties of Composites of Yb₁₄MgSb₁₁ with Iron. *ACS Appl. Energy Mater.* **2020**, *3* (3), 2147–2159. https://doi.org/10.1021/acsaem.9b02168.
- (50) Schlögl, R.; Loose, G.; Wesemann, M. On the Mechanism of the Oxidation of Graphite by Molecular Oxygen. *Solid State Ionics* **1990**, *43* (C), 183–192. https://doi.org/10.1016/0167-2738(90)90483-8.
- (51) Hayns, M. R. Molecular Orbital Calculations of the Chemisorption and Diffusion of Oxygen and Water on a Graphite Substrate. *Theor. Chim. Acta* **1975**, *39* (1), 61–74. https://doi.org/10.1007/BF00547787.
- (52) Pan, Z.; Yang, R. T. Strongly Bonded Oxygen in Graphite: Detection by High-Temperature TPD and Characterization. *Ind. Eng. Chem. Res.* **1992**, *31* (12), 2675–2680. https://doi.org/10.1021/ie00012a008.
- (53) Xu, Y. J.; Li, J. Q. The Interaction of Molecular Oxygen with Active Sites of Graphite: A Theoretical Study. *Chem. Phys. Lett.* **2004**, *400* (4–6), 406–412. https://doi.org/10.1016/j.cplett.2004.11.010.
- (54) Ohno, S.; Imasato, K.; Anand, S.; Tamaki, H.; Kang, S. D.; Gorai, P.; Sato, H. K.; Toberer, E. S.; Kanno, T.; Snyder, G. J. Phase Boundary Mapping to Obtain N-Type Mg₃Sb₂-Based Thermoelectrics. *Joule* **2018**, *2* (1), 141–154. https://doi.org/10.1016/j.joule.2017.11.005.
- (55) Ohno, S.; Aydemir, U.; Amsler, M.; Pöhls, J.; Chanakian, S.; Zevalkink, A.; White, M. A.; Bux, S. K.; Wolverton, C.; Snyder, G. J. Achieving ZT > 1 in Inexpensive Zintl Phase Ca9Zn4+ XSb9 by Phase Boundary Mapping. *Adv. Funct. Mater.* **2017**, *27* (20), 1606361. https://doi.org/10.1002/adfm.201606361.

- (56) Wood, M.; Toriyama, M. Y.; Dugar, S.; Male, J.; Anand, S.; Stevanović, V.; Snyder, G. J. Phase Boundary Mapping of Tin-Doped ZnSb Reveals Thermodynamic Route to High Thermoelectric Efficiency. *Adv. Energy Mater.* **2021**, 2100181. https://doi.org/10.1002/aenm.202100181.
- (57) Hu, Y.; Cerretti, G.; Kunz Wille, E. L.; Bux, S. K.; Kauzlarich, S. M. The Remarkable Crystal Chemistry of the Ca₁₄AlSb₁₁ Structure Type, Magnetic and Thermoelectric Properties. *J. Solid State Chem.* **2019**, *271*, 88–102. https://doi.org/10.1016/j.jssc.2018.12.037.
- (58) Toberer, E. S.; Cox, C. A.; Brown, S. R.; Ikeda, T.; May, A. F.; Kauzlarich, S. M.; Snyder, G. J. Traversing the Metal-Insulator Transition in a Zintl Phase: Rational Enhancement of Thermoelectric Efficiency in Yb₁₄Mn_{1-x}Al_xSb₁₁. *Adv. Funct. Mater.* **2008**, *18* (18), 2795–2800. https://doi.org/10.1002/adfm.200800298.
- (59) Goldsmid, H. J.; Sharp, J. W. Estimation of the Thermal Band Gap of a Semiconductor from Seebeck Measurements. *J. Electron. Mater.* **1999**, *28* (7), 869–872. https://doi.org/10.1007/s11664-999-0211-y.
- (60) Wei, T.-R.; Guan, M.; Yu, J.; Zhu, T.; Chen, L.; Shi, X. *How to Measure Thermoelectric Properties Reliably*; 2018. https://doi.org/10.1016/j.joule.2018.10.020.
- (61) Zhu, H.; Mao, J.; Li, Y.; Sun, J.; Wang, Y.; Zhu, Q.; Li, G.; Song, Q.; Zhou, J.; Fu, Y.; et al. Discovery of TaFeSb-Based Half-Heuslers with High Thermoelectric Performance. *Nat. Commun.* **2019**, *10* (1), 270. https://doi.org/10.1038/s41467-018-08223-5.
- (62) Sakurada, S.; Shutoh, N. Effect of Ti Substitution on the Thermoelectric Properties of (Zr,Hf)NiSn Half-Heusler Compounds. *Appl. Phys. Lett.* **2005**, *86* (8), 082105. https://doi.org/10.1063/1.1868063.
- (63) Shutoh, N.; Sakurada, S. Thermoelectric Properties of the Ti_X(Zr_{0.5}Hf_{0.5})_{1-X}NiSn Half-Heusler Compounds. *J. Alloys Compd.* **2005**, *389* (1–2), 204–208. https://doi.org/10.1016/j.jallcom.2004.05.078.
- Zhang, H.; Wang, Y.; Dahal, K.; Mao, J.; Huang, L.; Zhang, Q.; Ren, Z. Thermoelectric Properties of N-Type Half-Heusler Compounds (Hf_{0.25}Zr_{0.75})_{1-x}Nb_xNiSn. *Acta Mater*. **2016**, *113*, 41–47. https://doi.org/10.1016/j.actamat.2016.04.039.
- (65) He, R.; Zhu, H.; Sun, J.; Mao, J.; Reith, H.; Chen, S.; Schierning, G.; Nielsch, K.; Ren, Z. Improved Thermoelectric Performance of N-Type Half-Heusler MCo_{1-x}Ni_xSb (M = Hf, Zr). *Mater. Today Phys.* **2017**, *1*, 24–30. https://doi.org/10.1016/j.mtphys.2017.05.002.
- (66) Zhu, H.; He, R.; Mao, J.; Zhu, Q.; Li, C.; Sun, J.; Ren, W.; Wang, Y.; Liu, Z.; Tang, Z.; et al. Discovery of ZrCoBi Based Half Heuslers with High Thermoelectric Conversion Efficiency. *Nat. Commun.* **2018**, *9* (1), 2497. https://doi.org/10.1038/s41467-018-04958-3.
- (67) Fu, C.; Wu, H.; Liu, Y.; He, J.; Zhao, X.; Zhu, T. Enhancing the Figure of Merit of Heavy-Band Thermoelectric Materials Through Hierarchical Phonon Scattering. *Adv. Sci.* **2016**, *3* (8), 1600035. https://doi.org/10.1002/advs.201600035.
- (68) Liu, Z.; Guo, S.; Wu, Y.; Mao, J.; Zhu, Q.; Zhu, H.; Pei, Y.; Sui, J.; Zhang, Y.; Ren, Z. Design of High-Performance Disordered Half-Heusler Thermoelectric Materials Using

- 18-Electron Rule. *Adv. Funct. Mater.* **2019**, *29* (44), 1905044. https://doi.org/10.1002/adfm.201905044.
- (69) Fu, C.; Zhu, T.; Liu, Y.; Xie, H.; Zhao, X. Band Engineering of High Performance P-Type FeNbSb Based Half-Heusler Thermoelectric Materials for Figure of Merit ZT > 1. *Energy Environ. Sci.* **2015**, *8* (1), 216–220. https://doi.org/10.1039/C4EE03042G.
- (70) Ohno, S.; Zevalkink, A.; Takagiwa, Y.; Bux, S. K.; Snyder, G. J. Thermoelectric Properties of the Yb₉Mn_{4.2-x}Zn_xSb₉ Solid Solutions. *J. Mater. Chem. A* **2014**, *2* (20), 7478–7483. https://doi.org/10.1039/C4TA00539B.
- (71) Ozen, M.; Yahyaoglu, M.; Candolfi, C.; Veremchuk, I.; Kaiser, F.; Burkhardt, U.; Snyder, G. J.; Grin, Y.; Aydemir, U. Enhanced Thermoelectric Performance in Mg_{3+x}Sb_{1.5}Bi_{0.49}Te_{0.01} via Engineering Microstructure through Melt-Centrifugation. *J. Mater. Chem. A* **2021**, *9* (3), 1733–1742. https://doi.org/10.1039/D0TA09993G.
- (72) Perez, C. J.; Cerretti, G.; Wille, E. L. K.; Devlin, K. P.; Grewal, N. S.; Justl, A. P.; Wood, M.; Bux, S. K.; Kauzlarich, S. M. Evolution of Thermoelectric Properties in the Triple Cation Zintl Phase: Yb_{13-x}Ca_xBaMgSb₁₁ (x = 1–6). *Chem. Mater.* **2021**, *11*, acs.chemmater.1c02584. https://doi.org/10.1021/acs.chemmater.1c02584.

TOC

